universität wien

MASTERARBEIT | MASTER'S THESIS

Titel | Title

Particle Number Size Distribution Measurements of Polyethylene Terephthalate Nanoplastic Particles in Compressed Air and Nitrogen

verfasst von | submitted by

Constantin Hobza BSc BSc

angestrebter akademischer Grad | in partial fulfilment of the requirements for the degree of

Master of Science (MSc)

Wien | Vienna, 2024

Studienkennzahl lt. Studienblatt	Degree programme code as it appears on the student record sheet:	UA 066 876
Studienrichtung lt. Studienblatt	Degree programme as it appears on the student record sheet:	Masterstudium Physics
Betreut von	Supervisor:	Assoz. Prof. Dr. Paul Winkler Privatdoz.

Acknowledgments

I want to express my sincere gratitude to Assoz. Prof. Dr. Paul Winkler for providing me with the opportunity to explore such a recent and important topic in the field of aerosol physics. His guidance and support really helped me face the challenges of this thesis. I am also very grateful that he proposed me as a speaker for the European Aerosol Conference, where I had the exciting possibility to present my master thesis to a large audience. It was a completely new and enjoyable experience that I am grateful for.

I also extend my appreciation to Dr. Peter Wlasits for his frequent assistance and guidance throughout my whole measurement process. His patience and support have been crucial to my progress. Without him, I would have never managed to complete my measurements successfully.

Additionally, I want to thank Christian Sommer for his support during the weeks Dr. Peter Wlasits was absent. It was nice to have a colleague to talk to and to discuss various occurring problems. I will surely miss our shared lunch breaks.

Besides that, I want to thank Ruth Konrat for helping me out whenever I could not find something in the lab. She always knew where to find it and also helped me with a few experimental problems.

Moreover, I would like to emphasize how engaging and fascinating my research in the field of aerosol physics has been for me. It is a field that constantly challenges us to think critically and find innovative solutions.

Abstract

The topic of micro- and nanoplastics in the environment has steadily increased its presence in the media over the course of the last years. While the problem of plastic waste in marine environments quickly turned into a big problem of the modern world with a lot of ongoing research, our understanding of micro- and nanoplastics in the atmosphere is still rather poor. While the transport mechanisms have already been investigated in some cases, we still lack a proper understanding of the overall generation mechanisms. In addition, both the detection and characterization of airborne micro- and nanoplastics are not possible in most situations. This work aims to find a set of parameters to properly characterize the aerosol particle generation of polyethylene terephthalate (PET) plastic by variation of the temperature, the flow rate and the initial sample amount in a tube furnace. For this research, two different PET plastics are used, a high purity version of which the composition is specified and a commodity version of unknown composition. Whereas the behavior of the two plastic samples is rather uniform when comparing them under air, a change of the carrier gas to nitrogen yields a significant shift of the peak of the particle number size distribution (PNSD) towards smaller particle diameters. Compared to nitrogen, the presence of an oxidative carrier gas has an additional effect on the discoloration process of the samples. Further measurements focus on the cutoff diameter of a condensation particle counter (CPC), yielding larger values for both kinds of plastic when using nitrogen gas instead of air.

Zusammenfassung

Das Thema Mikro- und Nanoplastik in der Umwelt hat in den letzten Jahren zunehmend an medialer Präsenz gewonnen. Während Plastikmüll ein wachsendes Problem für die Gewässer darstellt, wozu es bereits eine Vielzahl an Forschungsarbeiten gibt, ist unser Verständnis von Mikro- und Nanoplastik in der Atmosphäre noch recht gering. Obwohl die Transportmechanismen in einigen Fällen bereits untersucht wurden, fehlt uns dennoch das Wissen über den Entstehungsprozess. Darüber hinaus ist sowohl die Detektion als auch die Charakterisierung von luftgetragenen Mikro- und Nanoplastik Partikeln nahezu unmöglich. Diese Arbeit zielt darauf ab, Parameter zu finden, die die Bildung eines Aerosols aus Polyethylenterephthalat (PET) Kunststoffpartikeln angemessen charakterisieren. Das wird durch eine Variation der Temperatur, des Durchflusses und der Probenmenge von PET in einem Rohrofen erreicht. Für diese Arbeit werden zwei unterschiedliche PET Kunststoffe verwendet, eine hochreine Version, deren Zusammensetzung bekannt ist und eine handelsübliche Version unbekannter Zusammensetzung. Das Verhalten der beiden Kunststoffproben unter Luft zeigt sich einheitlich, während ein Wechsel des Trägergases zu Stickstoff zu einer signifikanten Verschiebung des Maximums der Partikelanzahl-Größenverteilung (PNSD) zu kleineren Partikeldurchmessern führt. Im Vergleich zu Stickstoff hat ein oxidatives Trägergas zusätzliche Auswirkungen auf den Verfärbungsprozess der Proben. Weiters werden Cutoff-Messungen mit einem Kondensationskeimzähler (CPC) durchgeführt, die für Stickstoff als Trägergas größere Werte für die Cutoff-Durchmesser beider Kunststoffarten ergeben als für Luft.

List of Abbreviations

CPC condensation particle counter

DMA differential mobility analyzer

FCE Faraday cup electrometer

PE polyethene

PP polypropene

PVC polyvinyl chloride

PET polyethylene terephthalate

cPET commodity version of PET

MP microplastic

NP nanoplastic

HEPA-filter high-efficiency particulate air/arrestance filter

PNSD particle number size distribution

AIM Aerosol Instrument Manager software from TSI

Contents

Chapter 1

Introduction

During the last years, the research for micro- and nanoplastic particles in the environment has been steadily growing. One reason is that the generation mechanisms have not been investigated to a point where we sufficiently understand them, especially on the smallest scale of nanoparticles [1].

Some research has already been done by [1] on the fundamental generation and characterization of nanoplastics, including polyethene (PE), polypropene (PP) and polyethylene terephthalate (PET) at comparatively low temperatures. The measurements yielded concentrations up to a few 10^7 particles per cm^3 in the range of 1 to 40 nm, especially for PET plastic. In addition, the results imply that the PET aerosol generation might be linked to thermal and thermo-oxidative degradation by oxygen from the air. [1]

As stated in [2], the environmental effects of micro- and nanoplastic particles in the atmosphere are mainly unknown. Thus, it is of great interest to reproduce the measurements with PET particles and to compare the generation of the aerosol in a nitrogen carrier gas. This way, it is possible to better understand the effects of a non-reactive, inert atmosphere on the particle formation process. A basic understanding of the possible differences of the resulting physical and chemical properties of the aerosol particles would enhance our incomplete knowledge when dealing with this topic.

Another crucial point is that the detection and characterization of airborne nanoplastics is still not possible [3]. This gives even more importance to the generation of a stable particle number size distribution (PNSD), as a basis for further research.

In addition, micro- and nanoplastics may have a negative effect on human health that might even lead to possible long-term damages [4, 5, 6, 7]. A sufficient understanding of the possible generation mechanisms is therefore an ideal basis to conduct further research in this field of study.

Therefore, the aim of this thesis is to investigate the behavior of the PNSD of PET nanoparticles in dependence of different temperatures of a tube furnace, different flow rates and different initial plastic sample masses. A high purity version of PET will be compared to the commodity version from plastic bottles.

The first step is to use compressed air and a tube furnace to generate PET plastic particles. After passing a condenser and a charger, the aerosol is led into a differential mobility analyzer (DMA). By ramping its voltage, it is possible to obtain a PNSD with a condensation particle counter (CPC) and a Faraday cup electrometer (Faraday cup electrometer (FCE)). While the CPC is the instrument of choice here, as it is perfect to give insight to PNSDs that span under 10 nm, the FCE is a reasonable reference instrument that measures regardless of particle size. It is useful, as the parallel monitoring allows for cut-off measurements of the CPC [8]. Both instruments will be used simultaneously at the output of the DMA to carefully monitor the PNSDs.

After the measurements with air, the experiment will be repeated with the exact same settings, this time using nitrogen as a carrier gas. If the particle generation is in any way linked to a thermo-oxidative degradation of the polymer chains of PET plastic [1], a possible outcome of the experiment could be a change of the PNSD. In addition to these measurements, the cutoff diameter of the CPC will also be evaluated for both kinds of plastic under the two different carrier gases. A possible discoloration of the plastics is also monitored. By comparing a single long heating process to multiple reheatings for both air and nitrogen gas, possible differences in the visual appearance of both kinds of plastic will be presented - yielding even more insight to a possible oxidative reaction of the plastic. [1]

Chapter 2

A General Introduction to Plastic

The term plastic is a rather general name for a material that comes in many different variations that are suitable for a broad range of applications in everyday life. However, there is one thing that they all have in common, and that is their chain-like structure. These big molecules are called macromolecules and as they consist of many smaller repeating components, called polymers. The single molecules of which the polymer is made of are called monomers. They can be thought of as fundamental building units for different kinds of plastics. [9]

In general, one can classify plastics into two distinct categories: thermoplastics and thermosets. [10]

Plastics of the first category - thermoplastics - have the convenient property that it is possible to melt them into any desired shape without changing their chemical structure. After cooling, they will hold the desired shape until they are heated up again, where they can be molded again into any shape. One can further subdivide them into amorphous resins, where their identifying feature is the fact that they do not have a short-range structure. A few examples of this group would be polystyrene, poly(vinyl chlorid) and poly(methyl methacrylate). [10]

The second subgroup of thermoplastics are semicrystalline resins. Their identifying feature is that they consist of amorphous and crystalline regions. A few examples of thermoplastics would be nylon, polyethylene and polyoxymethylene. [10]

On the other hand, there are so-called thermosets. These plastics change their chemical structure during the fabrication process. Therefore, it is not possible to reshape them, as a repeated heating would only lead to a degradation of the material. Polyurethane, polyester and epoxies are a few materials that belong into this group. [10, 11]

Regarding the possibility of reshaping thermoplastics over and over again, it is obvious that they are in fact the plastic type that can be recycled rather easily, when in contrast the thermosets cannot. [11]

The following section will specifically take a closer look at polyethylene terephthalate. Additionally, the terms microplastic and nanoplastic will be discussed, as well as the problem of plastic pollution in the environment and the corresponding health effects on wildlife and humans.

2.1 Polyethylene Terephthalate Plastic - PET Plastic

The plastic used in this work is exclusively polyethylene terephthalate plastic, short PET plastic. It is chemically a very stable polyester, often used for containers and packaging of food and drinks. A typical example are the well-known PET plastic bottles that many people use every day. Aside from that, one can also find this material recycled in fleece garments. [9]

Figure 1 shows the molecular structure of one monomer of PET. The big O denotes the oxygen atoms that are bound to the carbon atoms. Double lines indicate a double bond, while the ring in the middle is a benzene ring. The small n indicates that this monomer can be repeated multiple times to form the PET polymer. [9]

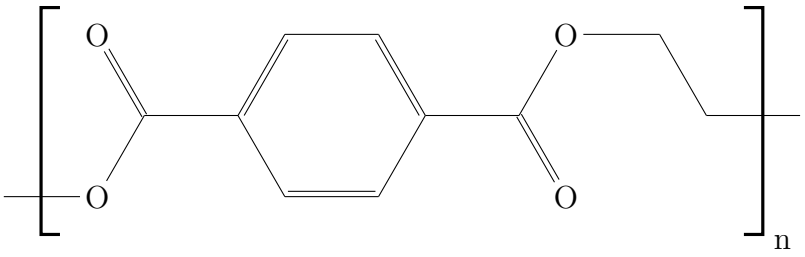

Figure 1: This sketch depicts the molecular structure of one single PET monomer. The subscript n denotes that this monomer can be repeated multiple times to form the PET polymer. Figure based on [9].

For this thesis, two different PET plastics are used. The first one is a standard high purity version of PET from the brand Sigma-Aldrich. The main thought behind this choice is that this plastic should be a great representative of the pure and clean PET plastic. However, this material is not free of additives, as it contains 30 % glass particles as reinforcer [12]. Table 1 summarizes the other important properties of this high purity PET version.

An important point is that the glass additives should propose no problem to the measurements here, as glass usually has a melting point over 600 °C, except for some exotic low-melting glass representatives [13]. As the temperatures used for the measurements of this thesis are in the range of 200-260 °C, it is a valid assumption that the added glass particles in the PET plastic should not interfere in any way with the measurements.

Table 1: Summary of the properties of the high purity PET plastic used throughout this work. It comes in a bottle from the brand Sigma-Aldrich in the form of small white pellets.

Chemical formula	$(C_{10}H_8O_4)_n$ [12]
Classification	thermoplastic [9]
Monomers	terephthalic acid, ethylene glycol [9]
Melting point/range	250 - 255 °C [12]
Density	1.68 g/cm^3 at 25 °C [12]
Physical state	granular (pellets) [12]
Additives	30 % glass particles (reinforcer) [12]

The second plastic type used for this thesis is a commodity PET version. It is simply harvested from a generic plastic bottle by using a hole puncher. The harvested samples are free of any label or glue. However, it is not possible to tell the specific composition of this plastic, since additives are very likely to be included.

For a better distinction of the two PET plastics, the high purity version will be denoted by the abbreviation PET, while the commodity version of PET will be indicated by the term cPET for the rest of this work.

2.2 Microplastic and Nanoplastic

There is no general definition of the terms microplastic (MP) and nanoplastic (NP). However, a reasonable division is that MPs fall in the range of approximately 5 mm down to 0.1 µm. Nanoplastics would then be all particles below this 100 nm threshold. [14]

For the term MP exist two major classifications: primary- and secondary MPs [15]. Primary MPs are specifically manufactured to be microscopic, they can be found in personal care and cosmetic products in the form of microbeads [16], for example.

The secondary MPs come from abrasion or fragmentation of initially bigger plastic pieces. This fragmentation comes from multiple natural factors, like wind or irradiation from the sun. As the polymer chains of many plastics absorb ultraviolet light, they undergo some photo-oxidative and thermo-oxidative reactions that may lead to the break-up of the material. [15, 17]

2.3 Plastic Pollution and Health Effects

Plastic pollution has become a global environmental challenge. This problem arose because the development of plastics was always focusing on the application rather than the end-of-life use. [18, 19]

In the year 2022, an amount of over 400 Mt of plastic was produced. This is an increase of over 8 % over the previous four years. However, still only a rather small fraction of the newly produced plastic comes from recycled materials. About 8.9 % stem from mechanically recycled material worldwide, in numbers these are 35.5 Mt. In the European Union (EU 27+3: member states + Norway, Switzerland and the UK), the mechanically recycled material reaches a level of 12.9 %, higher than the global mean. In [20, fig. 2] the increasing trend of plastic production over the years of 2018 to 2022 is visualized. [20]

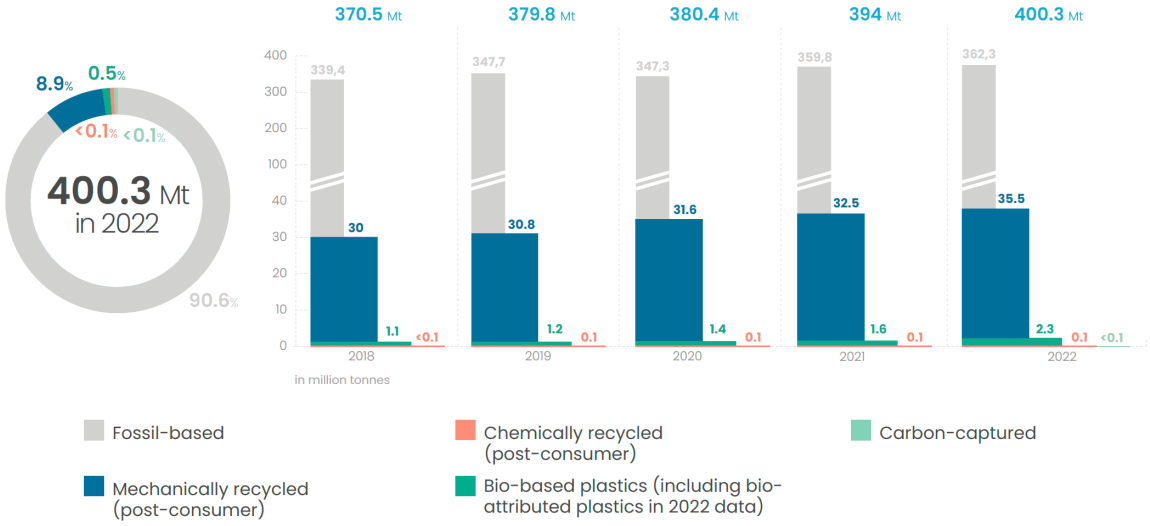

Figure 2: Plastic production from the years 2018 to 2022. Note the logarithmic scale on the y-axis. [20]

The main (global) amount of plastic material is PP with nearly 19 %, followed by PE and polyvinyl chloride (PVC). The contribution of PET plastic to the global plastic production adds up to 6.2 %. The area of application in the European Union falls mainly into two categories: packaging material (39 %) and materials for building and construction (23 %). This shows again the possible savings in plastic waste, if the packaging material, for example, could be reduced. [20]

The increasing rate of plastic production, its negligence and the mismanaged disposal of waste led to the accumulation of plastic debris in marine environments [18, 21]. It has been reported that a wide range of animals suffer under the effects of microplastic, such as sea turtles [22], sharks [23] and seabirds [24]. In one study, 58 drowned seabirds were

examined, and it was found that the majority of the species (73 %) had plastic particles in their digestive system [24]. There are two possible scenarios for the ingestion of the plastic: either they mistake it for prey, or they ingest it when feeding on their actual prey that has already been contaminated with MP. [24]

But the plastic problem is not only pertinent in marine environments, in fact MP has been found in the whole world so far [25]. It has been shown that it can even be found in the mountains - the Alps for example, as well as in remote and merely touched environments, like the Arctic [26] or in lakeshore sediments in the Tibetan Plateau [27]. One reasonable explanation for these findings is the atmospheric transport and the subsequent deposition of MPs through the air. [28]

Of course, all the phenomena described here also apply to humans, as MP also proposes a possible threat to us. As far as we know, there are a few possibilities of how plastic can enter our bodies. One obvious pathway is ingestion, the same as in the case of the already mentioned seabirds - the others are inhalation with following absorption into the lungs and absorption with our skin. [29]

While drinking water is apparently one of the main sources for MP ingestion, it has been found that water from bottles can have twice the amount of MP compared to tap water. Another typical source for MP is packaging material for food. Aside from the possibility of MP within it, there is also the problem of chemicals from the plastic that can intrude into the food, when being heated. This is a common problem of BPA (bisphenol A), for example, which is the reason for different diseases regarding the endocrine system. [29, 30]

The chemicals in plastic production are often so-called endocrine disruptors. Another name for them is hormonally active agents, they may cause disorders in the reproductive system, as well as various cancers. In addition, organic pollutants and heavy metals may also be transported by the MPs, thus contributing to further health issues. [30]

Regarding the digestive system, it has been stated that inflammation due to physical irritation is possible - this can lead to different gastrointestinal symptoms. Even the intestinal microbiome can be changed, leading to problems with harmful bacteria and the absence of beneficial ones, leading to abdominal pain or even vomiting. There are also severe effects possible on the respiratory system. After inhalation of MPs, a wide range of symptoms can occur. Inflammation inside the lungs can lead to dizziness and low concentrations of blood oxygen, as well as coughing and shortness of breath. Even mitochondrial damage in human respiratory cells is possible. [30]

In animal studies, it has been shown that MP can actually pass the blood-brain barrier. In the brain it can interact with neurons and have an influence on the cognition. [31]

While the versatile use of plastics provides numerous benefits for various industries, the waste production proposes significant challenges and extensive consequences. As presented, some examples include environmental pollution, ecosystem harm as well as threats to human health. All these points indicate the urgent necessity for a more efficient plastic management, as well as for new enhanced waste reduction strategies.

Chapter 3

Basic Theory and Concepts of Aerosol Physics

In the following sections, the most important physical concepts of aerosol physics will be reviewed. The topics presented will focus on nucleation theory, split up into homogeneous nucleation, as can be found in the tube furnace, and heterogeneous nucleation that is used in the working principle of the CPC.

Additionally, the theory behind the particle number size distribution, as well as the phenomenon of diffusion, that might play a role during the measurements in the tubing or in the instruments, will be presented. It is followed by the Cunningham slip correction factor, while the last section reviews the concept of the Reynolds number when dealing with laminar or turbulent flow conditions.

3.1 Nucleation Theory

When dealing with the topic of nucleation, it can be structured into two subcategories. The first is homogeneous nucleation, when there are no foreign substances in the primary vapor. Therefore, the nucleation only takes place onto the embryos that have formed from molecules of the vapor. In the other case, heterogeneous nucleation, foreign substances, particles or surfaces play an important role. They are the objects on which the nucleation process occurs. [32]

As homogeneous nucleation occurs in this thesis in the tube furnace and heterogeneous nucleation in the working principle of the CPC, it is mandatory to include it within this work. But as the focus of this thesis actually relies less on nucleation and more on the peculiarity of the measuring devices and the resulting comparison of the differences when using a non-oxidative carrier gas besides air, this subsection will only give an introductory summary, rather than an in-depth description of the topic of nucleation.

3.1.1 Homogeneous Nucleation

For homogeneous nucleation to arise, the corresponding vapor needs to be in the supersaturated (phase) state. It can be defined via the saturation ratio S, in dependency of the temperature T [32]:

$$S = \frac{p_A}{p_A^s(T)} \tag{3.1}$$

Here, p_A denotes the partial pressure, while $p_A^s(T)$ expresses the saturation vapor pressure at equilibrium where the liquid phase has a specific temperature, both corresponding to a solute A [32].

There are three possibilities for the value of S: if the ratio is lower than one, an unsaturated mixture is present. In the case equal to unity, a saturated mixture exists and for a value larger than unity, it is supersaturated. The excess value over the unity, denoted in percent, describes then the so-called amount of supersaturation [33]. One example would be that 5 % of supersaturation would indicate a saturation ratio of 1.05. A more familiar concept of the saturation ratio is expressed by [33], as explained in the form of relative humidity.

In the case of water vapor, the saturation ratio can be converted into relative humidity r_H by using the factor 100. Therefore, a saturation ratio of 0.7 corresponds to a relative humidity of 70 % - the same goes for a supersaturated mixture with $S = 1.2$ that corresponds to a r_H of 120 %. However, supersaturation barely exceeds a few percent in our normal environment.

Cooling a saturated vapor in the lab is one easy way to achieve supersaturation. A convenient approach that avoids generating temperature gradients is to use an adiabatic expansion of the vapor. To recap, an adiabatic process takes place without the interchange of any heat from the system to its environment. [33]

In the experiments of this thesis, homogeneous nucleation occurs in the condenser of the setup (see section 5.1). In the first step, the PET plastic is heated in the tube furnace to a specific temperature. The same goes for the carrier gas that collects the evaporated plastic in the tube furnace. It transports it out of the oven and into the condenser that is held on a constant low temperature (see section 4.1). As soon as the vapor enters the condenser, it starts to cool down rapidly due to the big temperature difference (about $\sim 200\,^{\circ}\mathrm{C}$). This induces homogeneous nucleation and condensation, resulting in a polydisperse aerosol. It is assumed that the whole procedure exclusively elapses in homogeneous nucleation, as the carrier gas should be free of any contamination due to the use of high-efficiency particulate air/arrestance filters (HEPA-filters) and a strict relative humidity monitoring ($< 10\,\%$ at all times).

To understand the relationship between the saturation ratio S and the radius of the so-called critical cluster r^*, the Kelvin equation is used. It has the form [32]:

$$\ln S = \frac{2\sigma v_l}{k_B T r^*} \tag{3.2}$$

The variable σ describes the surface tension, T the temperature and k_B the Boltzmann constant. The parameter v_l is an additional factor that describes the molar volume per molecule. As seen from equation 3.2, a particle needs to reach a specific radius r^*, in order to increase its size and become stable - under the supersaturated precondition of a given saturation ratio.

To briefly explain the concept of the critical radius r^*, one has to keep in mind that the change of the free-energy of the (growing/shrinking) cluster consists of two terms. In the first term, the increase of the free-energy due to surface area formation is described, while the second part characterizes the decrease of the free-energy, coming from a change in the chemical potential when switching from vapor to condensed phase. For a supersaturated vapor of $S > 1$, this trend has a maximum at a specific radius r^*, where any molecules added to the cluster make it energetically more favorable for it to grow in size. In contrast, any losses will lead to disintegration of the cluster. [32]

Experiments have shown that homogeneous nucleation can already occur at very low values for S, even lower than 10 for pure materials. This indicates that the whole nucleation process begins with particles larger than single molecules. Due to attractive forces like the van der Waals force between the vapor molecules, bigger clusters form all the time. As they are unstable for small values of S, they disintegrate all the time. For a higher supersaturation, the number of these clusters increases up to a point where the probability of a collision between them becomes so big that they eventually form a particle that exceeds the size r^*. In addition, the energy barrier and r^* decrease with increasing S, making it more likely for new clusters to overcome the energy barrier. At this point, it is possible for the particle to grow in size by condensation. The determining parameters are among others the particle size, the mean free path length and the saturation ratio. [33]

The specific point at which this phenomenon occurs is called the critical saturation ratio. It is clearly defined by the type of vapor and the corresponding temperature. As stated in [33], the homogeneous nucleation can be described as an all-or-nothing phenomenon - the resulting particle number distribution has very high concentrations of submicrometer particles in a relatively narrow, but polydisperse distribution.

3.1.2 Heterogeneous Nucleation

The second type of condensation, the heterogeneous nucleation, sometimes also called nucleated condensation, is far more common in nature - it is the most important mechanism involved in the formation of clouds. In contrast to homogeneous nucleation, it only takes a vapor with a few percent of supersaturation for heterogeneous nucleation to take place. If the nuclei are soluble, the formation of stable droplets is even possible below supersaturated conditions. [33]

A distinction can be made between three different cases, with the first highlighting the behavior of insoluble nuclei. In [33, p. 251], it is described in the following form: "At a given level of supersaturation, an insoluble nucleus with a wet-table surface will have an adsorbed layer of vapor molecules on its surface." If the radius of the particle is larger than r^*, it will grow by condensation, as the Kelvin equation holds also in the case of heterogeneous nucleation. For smaller particles, the growth mechanisms are rather complicated and depend on many different factors, such as their shape, surface structure or surface charge. [33]

The second case covers ions. In the atmosphere, ions are permanently created, either by the action of radioactive gases or the cosmic radiation. While these ions form clusters with a few tens of air molecules, they behave differently than the clusters explained in the previous subsection - they do not disintegrate all the time and are actually stable. They facilitate the nucleation above values of $S = 2$. However, in our atmosphere, particle formation and its subsequent growth is already common at lower levels of supersaturation due to the presence of numerous condensation nuclei. Therefore, ions can be interpreted as a negligible source for heterogeneous nucleation in the atmosphere. [32, 33]

The third case is in fact the most important mechanism in atmospheric nucleation: resulting particle formation from condensation on soluble nuclei. One prominent example are sodium chloride nuclei, commonly produced by ocean waves. It can be found all over the world - these particles are the main cause for the creation of water droplets in the atmosphere. Because of them, supersaturation in nature barely rises over a few percent. As soluble nuclei only need a supersaturation of a few percent to form new particles, they eventually lower the supersaturation as they use up all the excess vapor, thus preventing other mechanisms. [33]

The mechanism of heterogeneous nucleation can be exploited to measure number concentrations of aerosol particles. During the measurements of this thesis a so-called condensation particle counter is used. It utilizes a supersaturated working fluid, to grow initially small particles that cannot be detected optically. Due to heterogeneous nucleation, they increase their size to a couple of micrometers and can further be detected via an optical element. A more in-depth description about the working principle of a CPC will be given in section 4.4.

3.2 The Particle Number Size Distribution

When dealing with aerosols, it is advantageous to use an expression for the concentration per size interval. This gives a value that is described in terms of the particles sizes and the volume that the concentration is measured in. It is called the aerosol distribution and is denoted by n_i, where the index i stands for the size interval. In this case, the number concentration is proportional to the respective area under the concentration curve.

It can be described in the following way [32]:

$$n_i = \frac{N_i}{\Delta d_p} \quad \text{in} \quad \mu\text{m}^{-1}\,\text{cm}^{-3} \tag{3.3}$$

Here N_i denotes the absolute aerosol concentration and Δd_p is the interval for the respective size bin. To gain a more sophisticated description of the concentration, the interval of Δd_p can be reduced in size more and more. By finally using infinitesimally small intervals and taking the limit of $\Delta d_p \to 0$, one obtains:

$$\Delta d_p = \mathrm{d}(d_p) \tag{3.4}$$

Here $\mathrm{d}(d_p)$ is the infinitesimal small size bin element. Thus, it is possible to define the size distribution function as the concentration of particles per cm^{-3} in the carrier gas with diameters that lie in the range of the size interval $[d_p, d_p + \mathrm{d}d_p]$.

Therefore, the total number of particles per specific volume can be calculated by taking the following integral [32]:

$$N_t = \int_0^\infty n_N(d_p)\,\mathrm{d}(d_p) \tag{3.5}$$

By changing the upper limit of the integral to the value d_p and renaming the corresponding d_p inside the integral to d_p^*, as it is now a dummy variable, one can create an expression for the concentration of particles lower than a specific diameter d_p. The integral has the form [32]:

$$N(d_p) = \int_0^{d_p} n_N(d_p^*)\,\mathrm{d}(d_p^*) \tag{3.6}$$

Thus, by differentiating 3.6, the new form of the size distribution function is created:

$$n_N(d_p) = \frac{\mathrm{d}N}{\mathrm{d}d_p} \tag{3.7}$$

However, it is often more convenient to describe the particle diameter using the logarithm ($\log d_p$), as the aerosol size spectrum usually covers a wide range with several orders of magnitude of particle sizes. This proposes a mathematical problem, as the logarithm function can only be applied to a dimensionless variable. This is solved by using the basic arithmetic operations of the logarithm. Per definition, for each size bin d_p, there is a lower and an upper limit, $d_{p,low}$ and $d_{p,up}$, respectively. They can be used to cancel out the units in the logarithm:

$$\mathrm{d}\log(d_p) = \log(d_{p,up}) - \log(d_{p,low}) = \log\left(\frac{d_{p,up}}{d_{p,low}}\right) \tag{3.8}$$

With this in mind, the size distribution in formula 3.7 changes to the form shown below. This is the form of the particle number size distribution used throughout this thesis. It is convenient because the size distribution function oftentimes follows a lognormal distribution, properly described by the derived form. Instead of using the abbreviation n_N, the term $\mathrm{d}N/\mathrm{d}\log(d_p)$ will be used in most cases, as it is more widely used.

$$n_N\left(\log(d_p)\right) = \frac{\mathrm{d}N}{\mathrm{d}\log(d_p)} \tag{3.9}$$

3.3 The Cunningham Slip Correction Factor

The Cunningham slip correction factor C_s corrects for particle sizes that reach the mean free path length of the carrier gas molecules. Practically, this factor is only significant for size ranges lower than roughly 20-30 µm, as it converges rapidly to 1 for bigger particles, as seen in [34, fig. 3]. The mathematical description of C_s in dependence of the particle diameter d_p is given by [34]:

$$C_s(d_p) = 1.0 + A \cdot \left(\frac{\lambda}{d_p}\right) + B \cdot \left(\frac{\lambda}{d_p}\right) \cdot \exp\left(-C \cdot \left(\frac{d_p}{\lambda}\right)\right) \tag{3.10}$$

The occurring coefficients A, B and C have the following values [34]:

$$A = 2.492$$
$$B = 0.84$$
$$C = 0.43$$

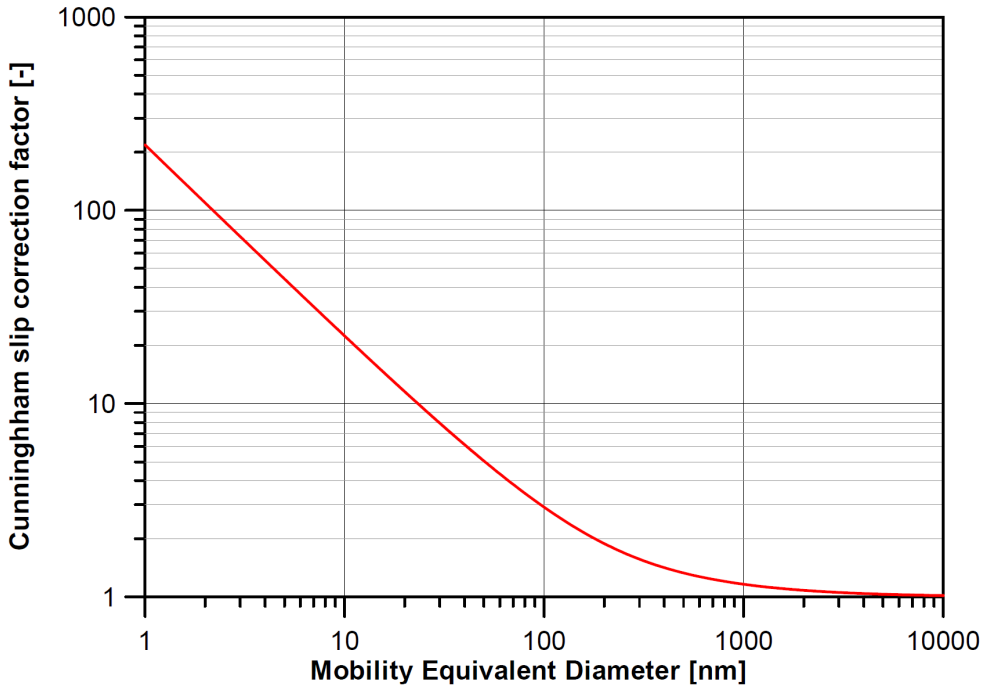

Figure 3: The trend of the Cunningham slip correction factor in dependence of different particle sizes in nanometers. [34]

The parameter λ denotes the mean free path length of the molecules in the carrier gas. As the experiments of this thesis focus on two different carrier gases, it is necessary to change λ, when switching from air to nitrogen. The exact values for the data evaluation, also including the values for the dynamic viscosity η for air and nitrogen, will be shown in section 5.3 of the Experimental Approach (chapter 5).

3.4 Diffusion

The irregular movements of an aerosol particle that is embedded in a gas is called Brownian motion. Its motion comes from the constant bombardment of the gas molecules. The resulting net transport of the particle is then called diffusion. This transport always takes place in a concentration gradient and moves particles towards a region of lower concentration.

The coefficient that characterizes this process is called D, the particle diffusion coefficient. A higher value indicates a faster diffusion and Brownian motion. It is defined via Fick's first law of diffusion [33]:

$$J = -D \cdot \frac{\mathrm{d}n}{\mathrm{d}x} \tag{3.11}$$

J is called the flux, describing the number of aerosol particles that travel each second through a unit cross-section. The other parameter $\mathrm{d}n/\mathrm{d}x$ describes the gradient of the concentration. In the case of aerosol particles, the diffusion coefficient can be described through the Stokes-Einstein derivation. It is formed by equating the force that acts on the particles due to diffusion to the force that comes from the gas in its way. These gas molecules resist the movement of the aerosol particle, thus exerting a resisting force on the movement of the particle. It can be described vie the Stokes drag equation, here denoted by F_{diff}, as the Cunningham slip correction factor C_s is also introduced into the diffusion equation [33]:

$$F_{diff} = \frac{3\pi\eta v d_p}{C_s(d_p)} \tag{3.12}$$

The variable η describes here the dynamic viscosity and v is the velocity of the (spherical) particle with diameter d_p when moving through the fluid. It dates back to Einstein that the net osmotic pressure force can actually be used to describe the diffusion force that acts on a particle [33]. The best way to visualize it is by using a semipermeable membrane in a liquid. Its descriptive characteristic is that it allows the molecules of the liquid to pass through unhindered, while it stops dissolved molecules. If the membrane is free to move, a force is necessary to keep it in its place. The force acting on the membrane comes from the osmotic pressure that forms due to the high concentration of the molecules that are dissolved in the liquid on one side of the membrane. In fact, the difference in the concentration is used to describe the occurring force, as it is directly proportional to it. [33]

This whole concept works not only for molecules that are dissolved in liquids, but also for aerosols - particles that are suspended in gases. It is described via the Van't Hoff equation for n molecules or particles that are suspended in a unit volume [33]:

$$p_0 = k_B T n \tag{3.13}$$

It includes the osmotic pressure p_0, the Boltzmann constant k_B and the temperature T. By taking some considerations regarding the diffusion in a confined space and using both formulas 3.12 and 3.13, the so-called Stokes-Einstein equation can be derived, that describes the diffusion coefficient D of an aerosol particle [33]:

$$D = \frac{k_B T C_s(d_p)}{3\pi\eta d_p} \tag{3.14}$$

This formula depicts, that D, given in units of $\mathrm{m^2\,s^{-1}}$, is inversely proportional to the square of the particle diameter d_p^{-2}, if the Slip Correction Factor is significant, like for small particles. For bigger particles, however, C_s can be neglected, as it converges towards one (see section 3.3). This implies that the diffusion coefficient is now only inversely proportional to the diameter (d_p^{-1}).

3.4.1 Diffusion in Sampling Lines

Particles in sampling lines will diffuse towards the walls and deposit there. One can think of the walls of the tube as areas with a particle concentration of zero, thus establishing a gradient and leading to diffusion. A general expression for the diffusive particle loss in a tube with a defined flow is given by the transport efficiency $\eta_{tube,diff}$ [35]:

$$\eta_{tube,diff} = \exp\left[-\xi \cdot Sh\right] \tag{3.15}$$

Sh stands for the Sherwood number and is a dimensionless coefficient for the mass transfer. It contains per definition the diffusive deposition velocity V_{diff} [35]:

$$Sh = V_{diff} \cdot \frac{d_p}{D} \tag{3.16}$$

By taking the assumption that the flow in the tubing is laminar at all times (see section 3.5), the Sherwood number can be defined via the following equation [35]:

$$Sh = 3.66 + \frac{0.2672}{\xi + 0.10079 \cdot \xi^{1/3}} \tag{3.17}$$

The variable ξ indicates in this formula the same parameter as in equation 3.15. It contains the relationship between D, the corresponding tube length L of the sample line and the volumetric flow rate, denoted by Q [35]:

$$\xi = \frac{\pi D L}{Q} \tag{3.18}$$

By applying these formulas to the setup of this thesis under air as carrier gas, it is possible to obtain an estimation regarding the losses in the tubing. For the sake of simplicity, the calculation will only be done for the tubing that connects the splitter at the end of the differential mobility analyzer with the condensation particle counter. This connecting piece is by far the longest tubing used (see section 5.1 regarding the setup), it consists of conductive tubing and has a length of $L = (15.50 \pm 0.50)\,\mathrm{cm}$. The aerosol flow has a value of $Q = (1.50 \pm 0.20)\,\mathrm{lpm}$.

Together with the room temperature of about 23 °C, the calculation is executed by using standard values for both, the viscosity η and the mean free path length λ, in air [36]. The graph is displayed in figure 4.

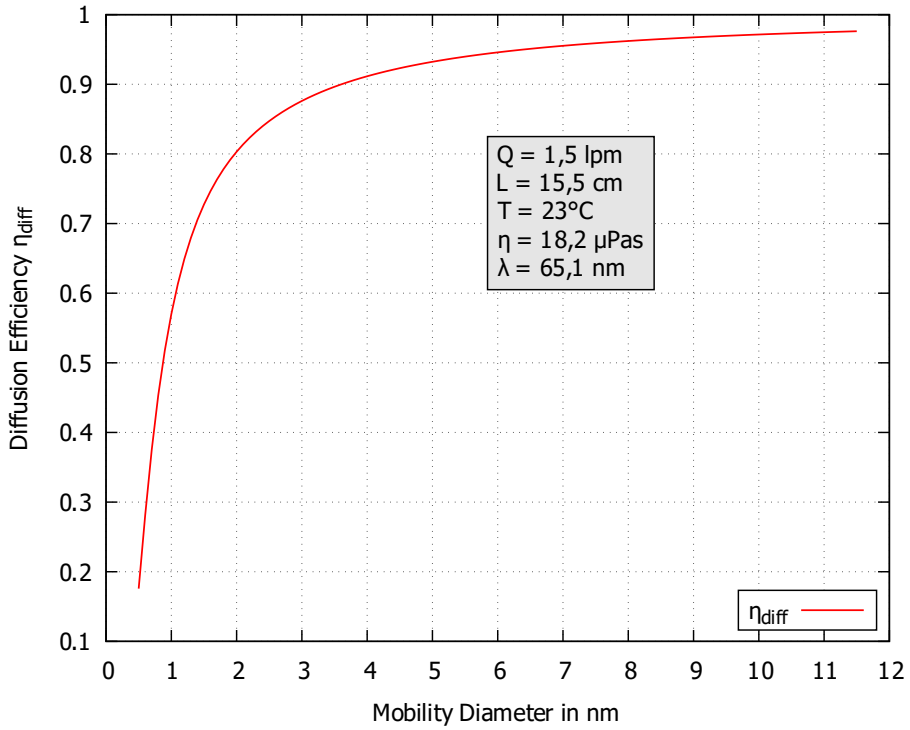

Figure 4: Diffusion efficiency for the tubing that feeds into the CPC. The curve is calculated for air as carrier gas, with the values for the viscosity η and the mean free path length λ coming from [36] for an ambient pressure of 1013.25 mbar. By changing η and λ to the corresponding values for nitrogen as the carrier gas, no visible change occurs in the graph.

A second calculation is done, this time using η and λ for nitrogen gas [36]. But due to the small difference in both values, the new obtained graph is indistinguishable from the graph for air. Its deviation lies within the thickness of the plotted line.

By inspecting the graph, one can see that the diffusion efficiency reaches a value of over 90 % for particles with a diameter larger than approximately 3.5 nm. We will see in section 5.4 later, that due to the cutoff diameter of the CPC, a correction regarding the diffusion efficiency would not impose a significant improvement of the measured data.

3.5 The Reynolds Number

In order to obtain information regarding the aerodynamic characteristics of aerosol particles, the notation of the Reynolds number is convenient. It yields a dimensionless value that specifies the motion of a fluid flow, either around an obstacle or through a tubing. According to [33], the properties of the Reynolds number can be summarized in three points:

- It distinguishes between the laminar and turbulent flow regime.
- It forms the ratio of inertial forces / frictional forces, thus hints which flow resistance equation to use.
- A similar value of the Reynolds number around a geometrically similar object indicates a similar streamline pattern (for different fluids / different sizes of the object).

As stated in the second point, the equation for the Reynolds number is obtained via setting the inertial force in relation to the frictional force by introducing the variable L as a measure for some characteristic length. For calculations around a spherical object, L can be the diameter of the particle. In the case of sampling lines, we need to consider a characteristic length of a cylinder, also given by its diameter. [33]

Additional knowledge about the density ρ of the fluid and v, the relative velocity between the object and the fluid, is also necessary, as well as the dynamic viscosity η. The equation has the following form:

$$Re = \frac{\rho v L}{\eta} \tag{3.19}$$

To find out if the flow regime is still laminar, it depends on the circumstances. In the case of a spherical particle that moves within the gas, a value of $Re < 1$ indicates the laminar flow regime with smooth streamlines. Smooth means that they are symmetrical upstream and downstream of the particle and form no eddies. If the particle enters the turbulent flow regime, where the eddies become gradually vigorous downstream, the Reynolds number increases to a value over one.

For a laminar flow within a tubing, like the sampling lines, the Reynolds number needs to have a value smaller than 2000 to call the flow properties laminar. However, it is important to highlight that these values indicate no strict border that separates the laminar from the turbulent flow regime - they only function as guiding values. In case of a flow within a cylindrical shape, the turbulent regime begins at Reynolds numbers > 4000. The differences of the guiding values for laminar conditions for tubings and particles stem from the difference in the importance of the inertial force for each case. [33]

Applied to the previous subsection regarding the diffusion in sampling lines (subsection 3.4.1), it is safe to say that the formulas for laminar flow conditions are applicable. After all, the Reynolds numbers for the carrier gases air and nitrogen, in the setup considered here, both lie at values between 300 and 400. For sampling tubings, a value smaller than 2000 is sufficient to assume laminarity.

Chapter 4

Instruments

This chapter aims at the detailed physical explanation of the main instruments used for the experiments of this thesis. The corresponding setup is shown in figure 11 in the following section of the experimental approach (chapter 5).

The next sections will cover the working principle of the tube furnace in which the PET plastic is vaporized, the radioactive Americium-241 charger and the differential mobility analyzer. Regarding the measuring devices, the basics of the condensation particle counter as well as the Faraday cup electrometer will also be explained.

4.1 The Tube Furnace

For the particle generation, a so-called tube furnace is used. It basically consists of a heatable body in cylindrical shape that has a hole in it. In this hole, a glass tube can be inserted. The walls of the furnace heat the glass tube up to a desired temperature that is set on the display of the instrument.

The sample material can then be inserted on a glass crucible into this glass tube for taking the measurements. This is done after the tube furnace reaches a stable temperature level because some measurements are rather close to the melting point of the plastic sample material. As the tube furnace generally overheats, sometimes up to 10 °C, this could potentially lead to a melting of the sample onto the glass crucible, which is not desired.

By connecting the glass tube to the desired carrier gas on one side, the carrier gas blows over the heated sample and transports its vapor further towards the colder region and the exit of the tube furnace. A simplified sketch of its basic composition is shown in figure 5.

The drop in temperature induces homogeneous nucleation and condensation. To make sure that a sufficiently high concentrated polydisperse aerosol is generated, a so-called Liebig-type condenser is put right behind the exit of the tube furnace. This condenser is cooled to

a fixed lower temperature than the tube furnace. While the temperature of the tube furnace for this work is typically in the temperature range of 200 - 260 °C, the condenser is statically held at a fixed temperature of 15 °C throughout all measurements. It basically consists of a double-walled glass tube - the colder temperature is then achieved by a water cooling system that flows between the walls.

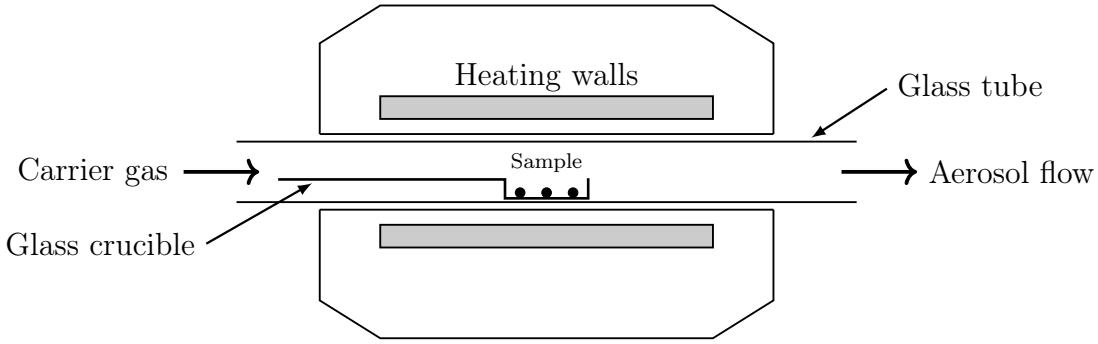

Figure 5: Schematic sketch of a tube furnace. The sample is positioned on a glass crucible and inserted into the glass tube of the furnace. It is heated by heating walls that surround the central area of the tube furnace. Figure based on [37].

4.2 The Charger (Am-241)

For further analysis of the aerosol, a proper charging mechanism is necessary, as not only the differential mobility analyzer, but also the Faraday cup electrometer relies on a well-defined charging state of the particles. There exist a few possible charger designs, with the most common being the radioactive bipolar diffusion charger [38].

The working principle relies on a radioactive source such as krypton (Kr-85), polonium (Po-210) or americium (Am-241) [38]. The latter is the chemical element used in the charger type of this thesis (americium charger). Americium itself is an alpha emitter that decays to neptunium (Np-237) via an α-particle with 5.5 MeV and some γ-rays [38].

Coming from the air in the charger, bipolar ions are created by the radioactive material. These ions collide due to electrostatic forces and the Brownian motion with the aerosol particles in the stream, hence called (bipolar) diffusion charging. The term bipolar indicates that there are ion molecules of both polarities present. The advantage of bipolar diffusion charging (in contrast to unipolar diffusion charging) is that it produces less multiply charged particles. However, it also has a lower charging efficiency. [38]

As the ions in the bipolar diffusion charger permanently compete in charging with both polarities, a steady-state equilibrium arises. This is the charge distribution that is visible as the output of the instrument. Conveniently, the initial charge distribution of the aerosol does not exert any trend on it - the resulting charge distribution is therefore independent of it. Figure 6 shows a schematic sketch of the basic structure of the americium charger. [39]

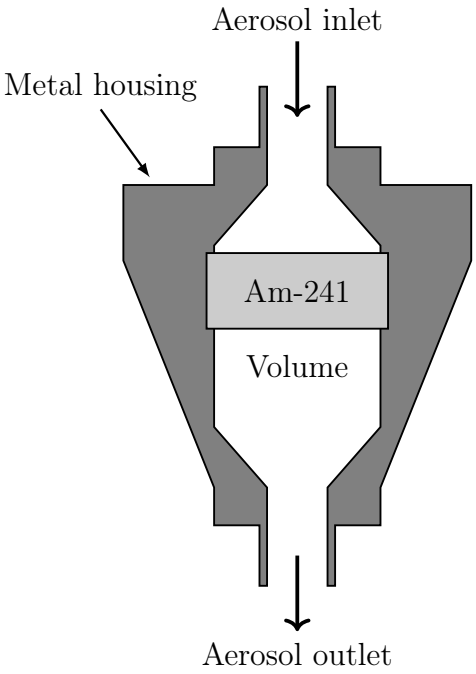

Figure 6: Schematic sketch of the Am-241 charger. Inside of the metal housing, a strip of americium-241 is placed. In the volume of the charger bipolar diffusion charging takes place. Figure based on [40].

4.2.1 The Wiedensohler Approximation

A detailed description of the charge distribution model is given by the famous work of Fuchs from the year 1963 [39]. It explains the collision of particles with ions that change the particle's neutral state towards charged, or vice versa. However, this calculation of the charging probabilities can get quite cumbersome. Thus, it is very convenient to use an approximation formula that has been derived by Wiedensohler in the year of 1988 [41]. This equation can be solved analytically and holds specifically for the case of a bipolar charge distribution [34]. The approximation formula has the following form [41]:

$$f(N) = 10 \hat{} \left[\sum_{i=0}^{5} a_i(N) \cdot \left(\log \frac{d_p}{\mathrm{nm}} \right)^i \right] \tag{4.1}$$

This formula holds in theory for a few different scenarios for the parameter N, the number of elementary charges on one particle. During this thesis, a charging state of $N = -1$ is given, thus leaving this approximation valid for particle sizes d_p in the range of 1 to 1000 nm. The corresponding coefficients a_i are all given by: [41]

$$\begin{aligned} a_0 &= -2.3197 & a_3 &= -0.1105 \\ a_1 &= 0.6175 & a_4 &= -0.1260 \\ a_2 &= 0.6201 & a_5 &= 0.0297 \end{aligned}$$

To illustrate the trend of the charge distribution after Fuchs, [34, fig. 7] shows how the charging probability behaves for different charges (in the picture denoted by i). It demonstrates why it is a valid assumption to neglect multiple charges during the measurements of this thesis: the charging probability of particles with double charge would need sizes bigger than approximately 50 nm to increase its value over 1 %. However, as the measurements span over the range of a few nanometers up to approximately 40 nm, the amount of multiple charged particles can be neglected.

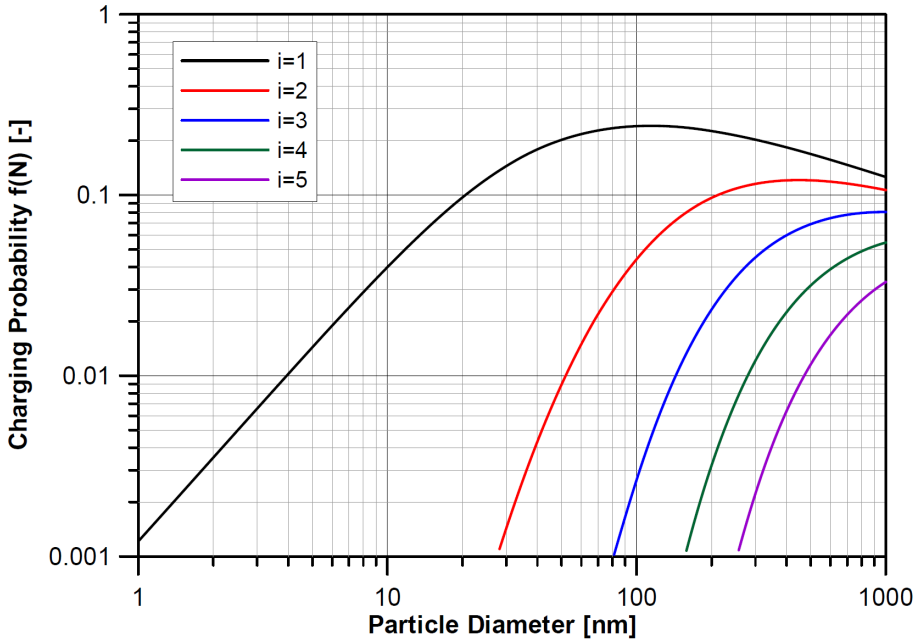

Figure 7: The charging probability after Fuchs, displayed for different negative charges i. [34]

4.3 The Differential Mobility Analyzer - DMA

To obtain a monodisperse aerosol fraction from a previously generated polydisperse aerosol, a differential mobility analyzer, short DMA, is used. It is the most crucial instrument for the setup of this work - it can be thought of as a big cylindrical capacitor. On the one hand, it can either sort out particles with one specific mobility when it is operated in a static voltage mode. On the other hand, it can be also used as an analyzing device when it ramps its voltage from high to low, giving information about the size distribution of the particles. [34]

The performance of the DMA relies on two distinct groups of parameters: the first group includes the fixed geometry parameters that are device-specific. As stated in [34, p. 30], they are: "R_1-outer radius of the inner electrode, R_2-inner radius of the outer electrode, L - effective axial distance between aerosol inlet and aerosol outlet" of the DMA. [34]

The second group contains the variable values for the operating conditions, such as the sheath air flow inwards ($Q_{sh,in}$) and outwards ($Q_{sh,out}$) of the DMA. Additionally, there are the aerosol sample flow rates Q_{in} and Q_{out} that describe the behavior of the flow that contains the aerosol. The parameters that hold for the used instrument of this thesis are summarized in table 2. As symmetrical flow conditions are created by a critical orifice in the sheath flow circuit, the in- and outgoing flow rates are assumed to be identical.

Table 2: Summary of DMA parameters under the assumption of symmetrical flow conditions.

R_1	R_2	L	$Q_{sh,in/out}$	$Q_{in/out}$
17.5 mm	24.1 mm	15 mm	24.9 lpm	3.2 lpm

In this thesis, a so-called Vienna type DMA, made of stainless steel, is used. Its special feature is that the filtered sheath flow is introduced tangentially and pressed through a laminarization mesh made out of nylon. The carrier gas with the aerosol is also introduced tangentially into the DMA. It is fed into an annular hollow space that distributes the aerosol evenly around the inner electrode, before it is introduced via a slit. The geometry of this slit ensures a smooth integration of the aerosol into the DMA with (ideally) no turbulent mixing. [34]

Inside the DMA, the charged particles of corresponding polarity drift towards the inner electrode. The applied voltage between the two electrodes can have a maximum value of +10 kV, therefore selecting only negatively charged particles. This value is the starting point for the voltage ramp downwards. The determining parameter of how fast the particles move is the electrical mobility (see subsection 4.3.1). Their path describes a line that connects the outer electrode via an axial and radial movement with the inner electrode. It directs the

particles to an annular exit slit at the bottom of the inner electrode. A schematic sketch in [34, fig. 8] explains the geometrical structure of the DMA and its belonging parameters visually. [34]

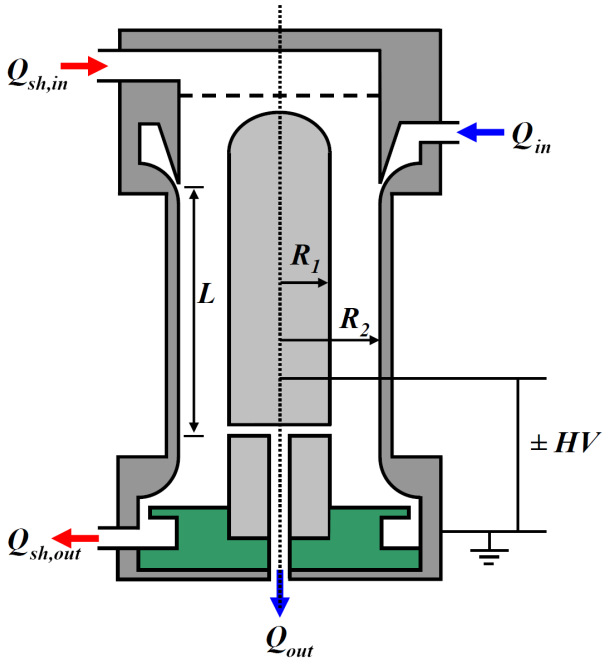

Figure 8: Schematic sketch of a differential mobility analyzer. Here, $Q_{sh,in}$ and $Q_{sh,out}$ describe the sheath flows inwards and outwards. The sample flows are denoted by Q_{in} for ingoing and Q_{out} for outgoing. Adapted from [34].

From the bottom of the inner electrode, the sorted aerosol is fed into the output tube of the DMA. The excess flow that contains some of the not filtered aerosol that did not impact on the inner electrode is led into the sheath flow output. From there, the residual flow is directed into a filter and back to the sheath flow pump.

Since the DMA is no ideal instrument, the slits both have a finite width, thus leaving room for a wider range of particles to enter during the measuring process. This can be described via the DMA resolution β, that holds under the condition of balanced flows and under the negligence of diffusion. This condition is assumed to be given at all times during the experimental process. The DMA resolution β is defined via the flows of the DMA in the following way: [42]

$$\beta = \frac{Q_{in} + Q_{out}}{Q_{sh,in} + Q_{sh,out}} \tag{4.2}$$

In the case of this work, the DMA resolution lies at 13 % for the assumption of symmetrical conditions. More details about the uncertainties of the measurements and the instruments will be explained in section 5.4.

4.3.1 The Electrical Mobility

The electrical mobility is the fundamental concept behind the functionality of a DMA. It describes the behavior how a charged aerosol particle with diameter d_p reacts to an external electric field E that exerts a force F_E on it. By staying in the Stokes regime, the electrostatic force can be equated to the Stokes drag. [33]

$$neE = \frac{3\pi\eta v d_p}{C_s(d_p)} \tag{4.3}$$

In this equation, n describes the number of elementary charges e. The other variables are the dynamic viscosity η, the particle velocity v due to the exertion of the force and the Cunningham slip correction factor C_s. By solving the term above regarding the velocity, one obtains the terminal electrostatic velocity v_{TE}. A part of the term can also be written by using the particle mechanical mobility B. [33]

$$v_{TE} = \frac{neEC_s(d_p)}{3\pi\eta d_p} = neE \cdot \frac{C_s(d_p)}{3\pi\eta d_p} = neEB \tag{4.4}$$

Using this equation, the electrical mobility Z of a charged particle with total charge $q = ne$ that moves in an electric field can be defined. It is given by the form [33]:

$$Z = \frac{v_{TE}}{E} = \frac{neC_s(d_p)}{3\pi\eta d_p} = neB \quad \text{for} \quad \text{Re} < 1 \tag{4.5}$$

Using this knowledge, it is possible to derive an expression for a DMA with known physical dimensions in relation to Z [34]:

$$Z = \frac{1}{2\pi LV} \cdot \frac{(Q_{sh,in} + Q_{sh,out})}{2} \cdot \ln\left(\frac{R_2}{R_1}\right) \tag{4.6}$$

L denotes the length of the electrode, V is the applied voltage and $Q_{sh,in}$ and $Q_{sh,out}$ denote the sheath flow inwards and outwards, respectively. While R_1 describes the outer radius of the inner electrode, the variable R_2 denotes the inner radius from the outer electrode. [34]

As all the parameters $L, Q_{sh,in}, Q_{sh,out}, R_1$ and R_2 can be assumed to be fixed during the measuring process, the only variable that will be changed is the voltage on the DMA. Therefore, a voltage ramp can be applied to sweep across a wide range of different electrical mobilities. To obtain a useful particle size from this electrical mobility values, one can rearrange equation 4.5 with respect to d_p:

$$d_p = \frac{ne}{3\pi\eta Z} \cdot C_s(d_p) \tag{4.7}$$

To recap, this formula only applies if the flow conditions inside the DMA are laminar, which is assumed to be given at all times. By using equation 4.6 for Z, a formula is created that can be used to calculate the equivalent mobility diameter d_p. However, this can only be done iteratively, since the Cunningham slip correction factor C_s also depends on d_p.

4.4 The Condensation Particle Counter - CPC

The condensation particle counter (CPC) is the instrument of choice to measure particles in the nanometer range. Because these particles are so small, any optical observation principle will fail for sizes $< 50\,\text{nm}$ [35]. Therefore the measurement procedure relies on the particle's growth. By using supersaturated vapor of a working fluid, the aerosol particles grow by heterogeneous nucleation and subsequent condensation up to a size that can easily be detected via an optical element. This size typically falls into the micrometer range and is near-uniform - practically independent of the initial aerosol particle sizes. Typically, CPCs can detect particles down to a few nm. [35]

The basic theoretical concept of all CPCs can be described in three phases: the first one is the supersaturation of the working fluid. In the case of this thesis, a water-based CPC is used. Another very common fluid would be butanol. The second phase involves the growth of the aerosol particles. This happens by the condensation of the vapor onto the particles. The third and last phase is the detection of the enlarged particles via some optical system.

For this thesis, the nano water-based condensation particle counter of the model TSI 3788 (N-WCPC) is used. It can detect particles with a lower limit of 2.5 nm with single-particle counting up to a concentration of $400\,000\,\text{cm}^{-3}$. It has two setpoints for the aerosol inlet flow: 0.6 and 1.5 lpm, where the latter is in use. A schematic picture of its working principle is shown in [43, fig. 9], it depicts the model 3788. [43]

The limiting factors of a CPC are in general its response time, the minimum detection limit and the losses that occur due to diffusion. Especially the diffusion losses can be a big source of uncertainty for particles in the lower nm range ($< 10\,\text{nm}$). To include all possible error sources and obtain a reliable estimation for the uncertainty of the measurements, a fixed error of 10 %, coming from its manual, will be used for any further error calculation with the data obtained from the CPC. [35, 44]

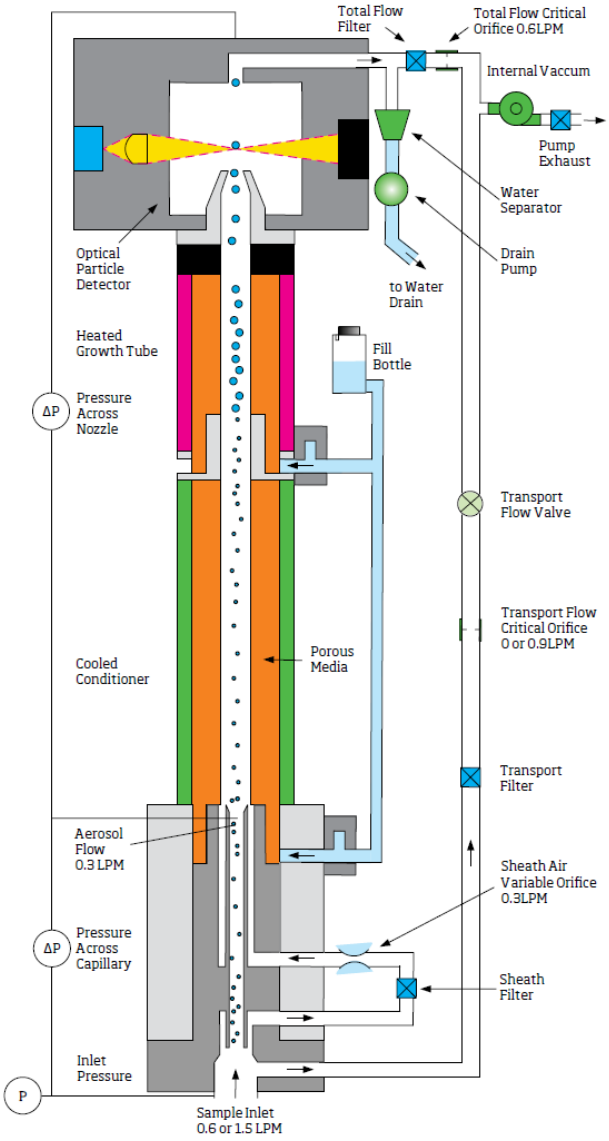

Figure 9: Schematic sketch of the CPC model 3788. [43]

4.4.1 The Cutoff Diameter

When taking measurements with a CPC, an important concept is the cutoff diameter. It is the lower size limit, at which the total detection efficiency of the instrument drops to 50 % [45]. Therefore, an instrument with a lower cutoff diameter is favorable for measurements, when the detection of small particles is crucial - the instrument can measure further down in the particle range. The total detection efficiency η_{tot} is defined via the product of a few parameters (after [46]):

$$\eta_{tot}(d_p) = \eta_s(d_p) \cdot \eta_a(d_p) \cdot \eta_c(d_p) \tag{4.8}$$

It consists of the sampling efficiency η_s, possibly governed by diffusion losses of small particles to the tubing walls. Then there is the fraction of activated particles, also called activation efficiency η_a. This also limits the CPC detection on the lower end of the size scale, as smaller particles will less likely be activated than larger ones. Additionally, hydrophilic particles will be activated more than hydrophobic, as the CPC used in this thesis is water based. The third parameter describes the efficiency of the internal detection mechanism, but to not confuse it with the total detection efficiency, one can also call it the counting efficiency η_c. This efficiency limits the detections due to coincidence counts for high concentrations $> 400\,000\,\mathrm{cm}^{-3}$. [44, 46]

A typical way to measure out the cutoff curve of a CPC is to use a Faraday cup electrometer (FCE - see next section 4.5) as a reference instrument. Thus, by taking the ratio of CPC over FCE and plotting it against the particle sizes, one obtains a characteristic curve that describes the detection efficiency of the CPC for the lower particle size range.

A convenient way to describe the behavior of the detection efficiency and the resulting cutoff diameter is the so-called Wiedensohler fit function. It can be described in the following form [41]:

$$f(x) = \frac{a}{1 + \exp\left(\frac{x - x_1}{x_2}\right)} \tag{4.9}$$

The parameter a describes the height of the plateau, with x_1 being the position where the efficiency drops to $a/2$. The third parameter x_2 describes the behavior of the slope. Via this fit parameters, it is possible to obtain the particle size for the 50 % cutoff diameter.

4.5 The Faraday Cup Electrometer - FCE

A Faraday cup electrometer, short FCE, is an instrument that detects electrically charged particles. It is made out of a filter that is encapsulated inside a Faraday cage. This Faraday cage consists of conducting material and is connected to an electrometer. As the aerosol in this thesis is already negatively charged, as selected by the DMA right after the radioactive Am-241 charger upon arrival at this instrument, it is a convenient addition to the CPC. In figure 10, a schematic sketch for the FCE is shown.

As the electrically charged particles enter the metal shield of the instrument, they reach the filter that lies inside the Faraday cup. The collected particles induce an electric charge in the Faraday cup, as it tries to isolate the internal electric field. This charge equals the charge on the particles. An electrometer, connected to the Faraday cup, keeps track of the current. The desired particle number concentration N in cm^{-3} can then be set into relation to the measured current I in A. [35]

Together with the elementary charge e ($1.602 \cdot 10^{-19}$ C), the charge amount n per particle (assumed to equal 1) and the flow Q_{FCE} ($\mathrm{cm^3\,s^{-1}}$) of the instrument, the formula takes the following form [47]:

$$N = \frac{I}{e \cdot n \cdot Q_{FCE}} \tag{4.10}$$

As the detection currents of a FCE are typically far below 100 fA [35], one has to use this instrument with special caution related to other influences that might stem from a lab. For a proper measurement, humidity, radio-frequency interference, any variations of electric fields, as well as mechanical vibrations should be avoided as good as possible [35]. After all, the electric output signal of the instrument is a composition of the outer-source signal (desired measurement) and an offset signal. This offset signal comes from internal disturbances of the instrument and has typically a value in the range of a few fA. It is no fixed offset value, in fact, it can be sensitive to the experimental conditions and can drift in the case of changing parameters, such as humidity or temperature. This is the reason why stable, non-disturbing measurement conditions are mandatory for the operation of a FCE. [48]

Due to all these facts, the FCE is the perfect instrument when it comes to measuring high aerosol particle concentrations, while low concentrations will inevitably get lost in the background noise. Therefore, it is a great addition to a CPC which can easily detect single particle counts, but has problems with coincident counts for high particle concentrations.

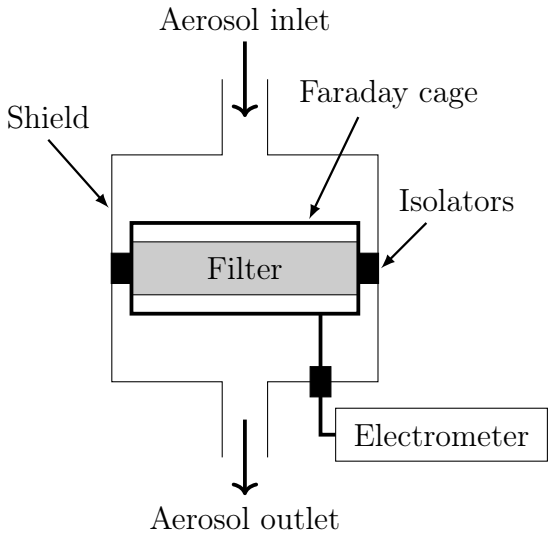

Figure 10: Schematic sketch of a Faraday cup electrometer. While the filter collects the charged particles, the current that comes from the induced charge on the Faraday cup is measured via an electrometer. Figure based on [35].

Another point that could propose a further problem for the measurement would be multiple charges. However, in [49] it is stated that for bipolar charging (that is indeed used for this thesis) measurements with particles smaller than 30 nm are not limited by this problem. As practically all peaks from the PNSD measurements will fall below this threshold, this problem can be neglected.

The specific type of FCE used for the experiments of this thesis is the TSI aerosol electrometer model 3068B. It has a wide particle size range that spans from 2 nm up to 5 µm with a sensitivity of ± 1 fA. It is temperature stabilized for a significant lower drift and has an automatic flow control when an external pump for the vacuum is used. [47]

Chapter 5

Experimental Approach

This chapter aims to give an in-depth summary of the experimental approach for the measurements, starting at the experimental setup and highlighting the differences for air in contrast to nitrogen as the carrier gas. The measurement procedure will also be addressed, as well as the data inversion via the Python script. Finally, the possible sources of uncertainties, the sample weighing and some FCE calibration measurements are presented.

5.1 Experimental Setup

5.1.1 Setup for Air as Carrier Gas

The experimental setup is basically an electrical mobility spectrometer, which consists in its main components of a charger, a DMA and a CPC/FCE. The schematic setup is shown in figure 11. The arrows on the lines denote the flow directions, all tubes used after the tube furnace in the setup are made of either metal or conductive tubing.

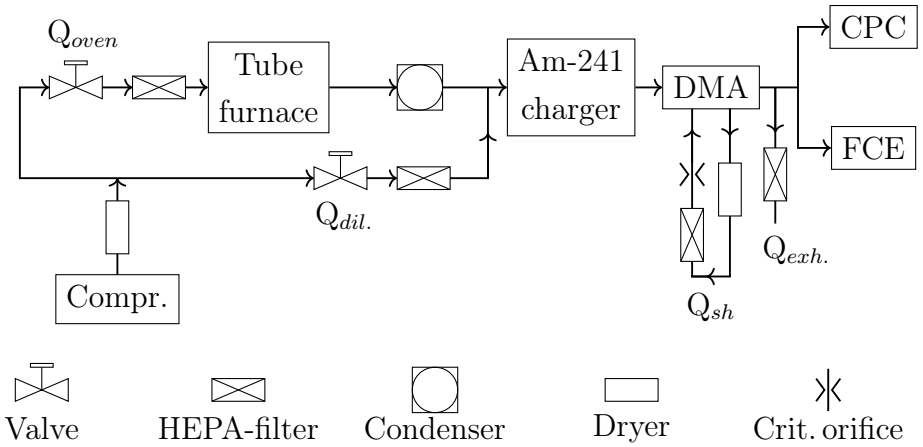

Figure 11: Schematic drawing of the experimental setup for the measurements done with air as carrier gas. Setup based on [1].

The air used in this setup comes from a compressor, where the air is already dried and subsequently passes a pressure reducing valve. Nonetheless, a silica gel dryer is used in front of the splitter, where the air is separated into two pathways, each controlled with a separate valve. After both of them, a HEPA-filter ensures a particle-free carrier gas.

The upper flow in the sketch is denoted by Q_{oven}, as it is the flow that enters the tube furnace in which the plastic samples are inserted. Afterward, a condenser, fixed at 15 °C and cooled by water, initiates homogeneous nucleation in the gas. At this point in the setup, the dilution flow, denoted by $Q_{dil.}$, reconnects with Q_{oven}. This dilution flow is the lower part in the figure. It is necessary to keep a constant inlet flow on the DMA, though more information on this topic will be given below.

After the merging of the two flows, a radioactive americium (^{241}Am) charger is used to bring the aerosol into a defined state of charge. It is followed by the differential mobility analyzer. The sheath flow $Q_{sh,in/out}$ is fixed to a value of (24.9 ± 0.2) lpm using a critical orifice in the sheath flow circuit (nominal value 25.0 lpm). The setup of the inlet sheath flow consists of a pump, an active carbon filter (not depicted in fig. 11), a silica gel dryer and a HEPA-filter. The outlet part again utilizes a HEPA-filter, before the circuit closes on the pump again. For simplicity, the second HEPA-filter and the pump are also excluded from figure 11.

After the DMA, there is an overflow tube that leads to the exhaust. It is followed by a splitter that directs the flow to the CPC and the FCE, which are both connected to a laptop where all measurements are recorded via the Aerosol Instrument Manager software from TSI (AIM). From there, all data from the measurement is stored and can be exported for further data analysis.

Regarding the DMA, the sample inlet flow has to maintain roughly 3.2 lpm. This comes from the fact that both the CPC and the FCE use roughly 1.5 lpm, therefore releasing the excess 0.2 lpm aerosol into a HEPA-filter. This ensures that both measuring devices always have the exact inlet flow that they need for proper operation.

As the flow through the tube furnace is a parameter that will be changed to different values during the collection of the PNSDs, a second (dilution) flow is necessary to always maintain the discussed 3.2 lpm on the inlet of the DMA. This ensures the freedom to choose any desired value for Q_{oven} during the measurements.

5.1.2 Setup for Nitrogen as Carrier Gas

In the case of nitrogen as the carrier gas, the setup is basically identical to figure 11 from the last subsection. There are only two small adjustments necessary: the first one is that there is no dryer in use before the flow splits up into Q_{oven} and $Q_{dil.}$. As the nitrogen gas comes out of the gas pipe with a relative humidity of $< 2\,\%$, there is no need for a dryer.

The second adjustment is to remove the HEPA-filter in front of the tube furnace, as it introduces a drastic increase of the relative humidity of the gas. This problem could have been solved by using a different filter, however, at this time there was none available. Of course, it was checked if the nitrogen gas had any contaminating counts on the CPC, but it turned out that the gas was perfectly clean, thus usable without any additional filter.

This problem only occurs for nitrogen gas, because of its low humidity level. In the measurements with air, the change in humidity is a significant drop to under 10 %, but for a dry gas with $< 2\,\%$, the humidity is constantly increased with approximately a factor of two.

5.2 Measurement Procedure

5.2.1 Preparatory Measurements

The basic preparatory measurements are the same every day. They consist of a few important points:

- Flow measurements
- Relative humidity measurements
- Functionality check of the CPC and FCE
- Leak test of the setup
- Contamination check - background measurement of the tube furnace

The first point, after starting the compressor and the pumps used for the DMA circuit and the exhaust of the FCE, is to measure the flows at every position in the setup. For this task a gas meter is used. The different tubes can simply be plugged into the gas meter and will give the value of the flow with an uncertainty of $\pm 0.2\,\mathrm{lpm}$. For a more accurate result, the flows are taken over the period of three minutes.

The flows that have to be checked every day are: the inlet flow into the tube furnace Q_{oven}, the dilution flow $Q_{dil.}$ and the sum of both of them after they merge behind the condenser (Q_{sum}). This sum is the first point where a leak could be detected, as it is always tuned to be fixed at 3.2 lpm.

Then the sheath flow of the DMA has to be checked, this means two measurements, one for the inlet $Q_{sh,in}$ and one for the outlet sheath flow $Q_{sh,out}$. Both measurements are carried out with the gas meter connected in series in the DMA sheath flow circuit. This ensures that the DMA circuit is completely closed, thus leading to no loss or gain of air altering the measurements.

Afterward, the flow out of the DMA can be measured, it is denoted by Q_{DMA}. Again, the flow has to have its fixed value of 3.2 lpm. At this time, the CPC and the FCE are already running. The intake flow of the CPC (Q_{CPC}) is always set to 1.5 lpm, however, its measurement always yields a value of approximately 1.47 lpm. As the CPC has a non-tunable flow, the experiment has to run with this specific value. However, this proposes no problem, as the FCE instrument can be tuned to a desired intake flow. It was found that a setpoint value of 1.56 lpm on the FCE gave a stable intake flow of $Q_{FCE} = 1.47$ lpm. Of course, a zero offset with a HEPA-filter in front of the inlet of the FCE was done every day. In addition, the background counts on the CPC are checked similarly - by just plugging the HEPA-filter onto its sample intake tubing.

After this functionality check of both instruments, the DMA outlet is connected to the CPC and the FCE with one open exhaust end. The last step is now to measure the overflow to the exhaust $Q_{exh.}$ and to confirm that it has a value of approximately 0.2 lpm. With this measurement done, the flow measurements and the leak test are finished.

In addition to these flow measurements, the relative humidity is also checked every day during this initial setup phase. It is taken for the flows Q_{oven}, $Q_{dil.}$, $Q_{sh,in}$, $Q_{sh,out}$ and Q_{DMA}. The values are always below 10 %. As these measurements do not take long, they are always executed between the different flow measurements, when there is time left.

The last point is always to preheat the tube furnace to the desired setpoint temperature and to take one complete DMA voltage ramp. If no particles are detected on the CPC, this ensures that the setup should have no leak and that there is no contamination in the glass tube in the furnace.

For a proper measurement procedure, the clock from the DMA Raspberry Pi PC needs to be synchronized to both of the clocks from the CPC and FCE PC. This step is crucial to ensure that the timestamps given to the data also coincide for each given day.

Regarding the measurements with nitrogen as the carrier gas, the procedure is fairly similar. The biggest difference is that the system has to be completely flushed with nitrogen gas. In theory this is no big problem, but since the complete DMA sheath flow air also has to be changed, it takes some time. In addition, there is no instrument in the lab available that could detect the purity of the nitrogen gas within the setup. Therefore, a different approach has to be taken.

By measuring the relative humidity of the nitrogen gas that is coming directly from the main line (< 2 %) and taking it as a reference value, it is possible to monitor the replaced air in the whole setup. The relative humidity of the air in the system is never lower than approximately 4 %. Introducing the nitrogen gas into the system should lower therefore the percentage. Experimentally it is found that a time of approximately 30 min is enough to flush the complete system with the whole DMA sheath flow volume.

The other preparatory measurements stay the same, only the relative humidity check is changed to one measurement of the Q_{DMA} flow. A low value of this relative humidity ensures the proper flushing of the system.

5.2.2 Procedure for Data Acquisition

After the preparatory measurements, the proper data acquisition can begin. By inserting a specific amount of either PET or cPET plastic on a glass crucible, a timer is set to 30 min. This dwell time is necessary to heat the plastic up and to flush out any possible particles that might have contaminated the setup during the insertion of the glass spoon. The temperature of the tube furnace should already be stable at the desired setpoint temperature. In the case of nitrogen, the dwell time is additionally necessary for the flushing of the system.

After this dwell time, the first measurement starts. By ramping the DMA voltage from 10 000 V down, both the CPC and the FCE receive a signal that corresponds to a specific size bin - the respective voltage of the DMA. This voltage remains stable at a specific value for 8 s, afterward it is lowered. The 10 000 V are divided into 97 logarithmically equidistant size channels (bins). This number is in fact an arbitrary value that is pre-set on the DMA program, as it works perfectly for most measurements.

After one DMA voltage ramp cycle is finished after approximately 15 min, the second run starts. To check the stability of the distribution, three consecutive voltage ramps are taken. As the uncertainty of the CPC is $\pm 10\,\%$, a distribution is called stable, when the variation in the maximum concentration of the PNSD is lower than these 10 %. After a successful measurement, the data is exported from the laptop for further data analysis via a Python script.

The procedure for the cutoff measurements is different. As these measurements need to be done for a few fixed particle diameters, the corresponding voltage values need to be evaluated first. This is done by calculating the different voltages via the Python script to obtain measurement steps that cover the rise of the cutoff curve.

Each measurement starts with the collection of two minutes of background noise. The DMA is then set to one fixed voltage level, thus keeping the chosen particles at one specific size. This is also done for two minutes, then the measurement is stopped. This procedure generates measurement files for the CPC and the FCE that start with the background noise and then increase to a specific concentration level for one fixed particle diameter. By discarding the middle part, where the switching of the DMA voltage happens, the noise and the measurement data can both be averaged - the noise is afterward subtracted from the data. For the plots, the relation between CPC/FCE can be calculated and plotted against the corresponding particle sizes.

5.3 Data Evaluation via the Python Script

The data evaluation is mostly done via a self written Python script. As the focus of this work is not lying on the specific details of the script, this section will only give a rough overview of the schematic procedure that lies behind the code.

The first step is to bring the measurement data into a form that is suitable for further data analysis. The files of each measurement are sorted into folders with the respective dates as names and entitled with the used temperature, plastic type, etc. For each measurement, there need to be at least three distinct files: the DMA voltage logfile and the logfiles both of the CPC and the FCE. They are exported from the AIM software with their belonging timestamps for each data point. Additionally, a .txt file is created manually that summarizes all the relevant data for each day individually - it will be used for further calculations in the code and consists of:

- $Q_{FCE,set}$ - the setpoint of the FCE sample flow in lpm
- $Q_{FCE,acc}$ - the accurate (measured) value of the FCE sample flow in lpm
- $Q_{sh,in}$ - the DMA sheath flow inwards in lpm
- $Q_{sh,out}$ - the DMA sheath flow outwards in lpm
- t - the time, the DMA stays on one voltage level in seconds
- if daylight-savings-time is active/inactive (for correction of timestamps)

The next step is to read all files in via the Python script and to save them to a dataframe. The FCE data is corrected by the factor of the sample inlet flow offset - however, the FCE signal is always used as a guiding reference instrument. Its important use comes in the case of the cutoff measurements.

Both DMA sheath flow measurements (in and out) are averaged to obtain the value that will be used in the subsequent calculations. One of the most important parameters is t, the time duration that indicates how long the DMA is fixed to one voltage level before adjusting to the next one. As the DMA voltage is only changed in discrete steps of varying size, even a smooth PNSD will have visible steps in the raw data format.

These steps need to be averaged to obtain one significant value for each respective voltage. To eliminate potential errors that might come from the switching of the voltage, the first and last seconds of each measurement step are discarded. This is done by comparing the timestamps of the DMA file with the ones from the CPC and the FCE file. After the

successful averaging of the values, they are stored in another dataframe that can be plotted by the python program itself. This step is taken to get a first glimpse at the data and to detect possible inconsistencies of the measuring process.

Additionally, the data is written into an output file (.dat) for further processing. During this step, the raw counts of both instruments are converted into the $\mathrm{d}N/\mathrm{d}\log(d_p)$ distribution. The format of the data is chosen in such a way that it is suitable for graphical analysis via Gnuplot. While the CPC data is already corrected, the offset noise of the FCE is not yet subtracted. This is not implemented in the code, as the FCE data is only used as a visual reference for the PNSD measurements. Only in the case of the cutoff measurements, this correction will be applied.

Regarding the specific constants used for the voltage-to-size conversion, different values are used for either air or nitrogen. These values stem from [36] where they are summarized for a temperature of 20 °C for various kinds of gases. The mean free path length λ is given in units of $\lambda{\cdot}p$, thus it is necessary to divide it by an ambient (standard) pressure of 1013.25 hPa. The dynamic viscosity η is given in standard units, thus no conversion is necessary. This leaves the values λ and η for air and nitrogen, as shown in table 3, for the calculations of this thesis. [36]

Table 3: Parameters for the mean free path length λ and the dynamic viscosity η for both carrier gases. [36]

Gas	λ	η
Air	65.14 nm	18.2 µPa s
Nitrogen	64.15 nm	17.5 µPa s

5.4 Possible Sources of Uncertainties

Regarding the estimation of the corresponding uncertainties, a few assumptions have to be made. The first one would be that the position of the glass crucible in the tube furnace is always the same. Even though the length of the glass tube and the length of the glass crucible that are both inserted into the furnace are checked at every measurement, they can only be positioned within an uncertainty of approximately 5 mm. This comes from the fact that the carrier gas supply always has to be plugged in, thus changing the previous alignment.

But even if this could be done without any issues, the next problem are the samples themselves. While the cPET pieces actually stay at the position where they are put, the high purity pellets are of cylindrical shape and therefore roll on the glass crucible. This

makes it impossible to always remain at the exact same heating spot within the tube furnace. Another fact are of course the differences in the glass crucibles: some have a slightly thicker glass, and some are nearly double the length of the others. But due to a lack of different resources, there is no alternative. For the main measurements, two glass crucibles with very similar appearance are chosen.

The next possible source of errors is the tube furnace itself. While it is possible to heat it up to a desired setpoint temperature, the actual temperature at the position of the glass crucible is unknown. However, it should be very close, as the alignment of the sample lies in the middle of the tube furnace. Besides this fact, there is also the problem of the initial overheating when choosing a desired temperature. Depending on its ramp rate, the temperature of the oven will exceed the setpoint and then cool down to the respective temperature. The sample is usually inserted when the temperature has reached a stable value, sometimes still fluctuating within about one or two degrees. These considerations lead to an estimated uncertainty of the setpoint temperature of the tube furnace of about 5 °C.

The next significant source of uncertainty is the DMA itself. While the actual value of the sheath flow varied for every measurement day a little within the uncertainty of the gas meter, the mean value is taken to calculate the corresponding resolution. It takes a value of (24.9 ± 0.2) lpm which corresponds to a resolution of 13 %, as calculated by equation 4.2. This will be the corresponding value for the estimation of the uncertainty of the particle diameters.

Regarding the gas meter, an uncertainty of 0.2 lpm is assumed, which comes from its reading accuracy. A suitable flowmeter could definitely enhance the whole measurement process and yield more precise flow settings. However, during the time of the data collection, no such instrument was available.

The uncertainty of the concentration regarding the particle number size distributions comes from the CPC. As stated in its manual, measurements up to a maximum concentration of 400 000 cm^{-3} have an accuracy of 10 % [44]. In contrast, the FCE has a specified current accuracy of 2 % of the reading or ±5 fA, depending on which value is greater [47].

An additional point is the question, whether diffusion in the sampling lines from the DMA to the CPC/FCE should be included as a correction factor in the uncertainty analysis. As will be shown in section 6.4, the cutoff diameter of the CPC lies at a particle size of about 4 nm, thus only giving significant data points for sizes larger than approximately 5 nm. By taking a closer look at the curve of the diffusion efficiency (fig. 4), calculated for the sampling line into the CPC, the value of η_{diff} corresponds to over 93 % efficiency, constantly rising for larger sizes (> 97 % for sizes > 9.6 nm). Due to these considerations, no diffusion correction will be applied to the obtained results and uncertainties.

The cutoff diameter has an additional important role, as it yields a lower limit to the measured PNSDs. The upper limit is given via the voltage of the DMA. As the power supply only reaches 10 000 V, the largest limiting particle size is approximately 40 nm. Conveniently, all obtained PNSDs have their peak within these limits.

To ensure further proper data collection, the humidity of the carrier gas (air/nitrogen) is monitored at the beginning of every measurement day. This is done at each place in the circuit where it could have changed, for example from a possible leak. By keeping the humidity constantly under 10 % (most of the time even under 5 %), a proper functionality of both the CPC and the FCE is granted.

The last point that should be addressed is the surrounding room temperature. With the windows always closed, the air conditioning system is at the beginning of every measurement day set to a fixed temperature of 23 °C. Together with the condenser, always set to 15 °C, the assumption is taken that the surrounding parameters for the measurement devices are constant throughout the whole data collection process.

5.5 Masses of the Plastic Samples

While the masses of the PET/cPET plastic pieces play a minor role regarding most measurements, a proper weighing of them is mandatory. The whole process of acquisition will be explained in detail throughout this section.

As for most measurements a sample amount of three high purity PET pellets is used, the initial mass determination is conducted by weighing three pellets together several times with a high sensitivity scales. By taking a series of ten measurements, the mass of one single pellet can be evaluated accurately. As there is a whole bottle of pellets, three different pellets are taken for each measurement to obtain a suitable representation of a possible variation in the masses.

The same goes for the commodity cPET snippets. As this weighing was done prior to the actual measurements, it was not yet clear that for a standard measure five cPET pieces would be used. Of course, this has no impact at all on the data collection - the masses simply have to be extrapolated. As the snippets are self-made, some thicker pieces are excluded from the measurements. They probably stem from a different spot on the bottle, possibly the bottleneck, where the material is thicker. This leads to a more uniform distribution of the masses, with smaller belonging uncertainties.

In table 4, the obtained masses for both plastic types are summarized. The corresponding errors are not coming from the uncertainty of the scales, but rather from the standard deviation of the mean, as it is the determining factor. For convenience, the masses are calculated down to obtain the value of one single sample piece.

Table 4: Masses for the PET pellets and the cPET snippets. The column *amount* indicates how many of them are examined. Regarding the measurements for the equal masses, one can see that two PET pellets roughly equal the mass of five cPET pieces (see section 6.3).

Amount	PET	cPET
1	(25.8 ± 1.3) mg	(9.81 ± 0.71) mg
3	(77.3 ± 3.7) mg	(29.4 ± 2.2) mg

5.6 Measurements Regarding the FCE

To ensure a proper working behavior of the Faraday cup electrometer, two measurements are taken. The first one is the flow calibration measurement, which shows the trend of the real measured flow inwards to the FCE compared to the setpoint flow, see subsection 5.6.1.

The second measurement checks, if the FCE has a specific count range where its offset is small when comparing FCE and CPC counts. This is an important fact to keep in mind when choosing a suitable temperature on the tube furnace to get an appropriate amount of counts on the FCE when dealing with cutoff measurements (subsection 5.6.2).

5.6.1 Flow Calibration of the FCE

The analysis of the inlet flow of the FCE is done prior to the start of the main measurements. By setting multiple inlet values that span from 1 up to 5 lpm and checking the actual flow with the gas meter, a linear dependency can be plotted, as shown in figure 12. An uncertainty for the setpoint values is ignored, as a specification is not found in the manual. The actual measured flow rates, however, have the belonging value of the gas meter with ± 0.2 lpm.

In addition to the data points, an applied linear regression shown in red is added. For reference, a blue line, indicating the perfect one-to-one ratio, is also added to the figure. It shows that the offset can be ignored up to approximately 2.0 lpm. In this range, it is lower than the uncertainty of 0.2 lpm. For the used setup of this thesis, the flow rate of the FCE needs to mirror the value of the CPC, which equals 1.5 lpm. Therefore, the setpoint of the FCE is set onto a value of 1.56 lpm for all measurements, as it is found that this mirrors the flow of the other device best.

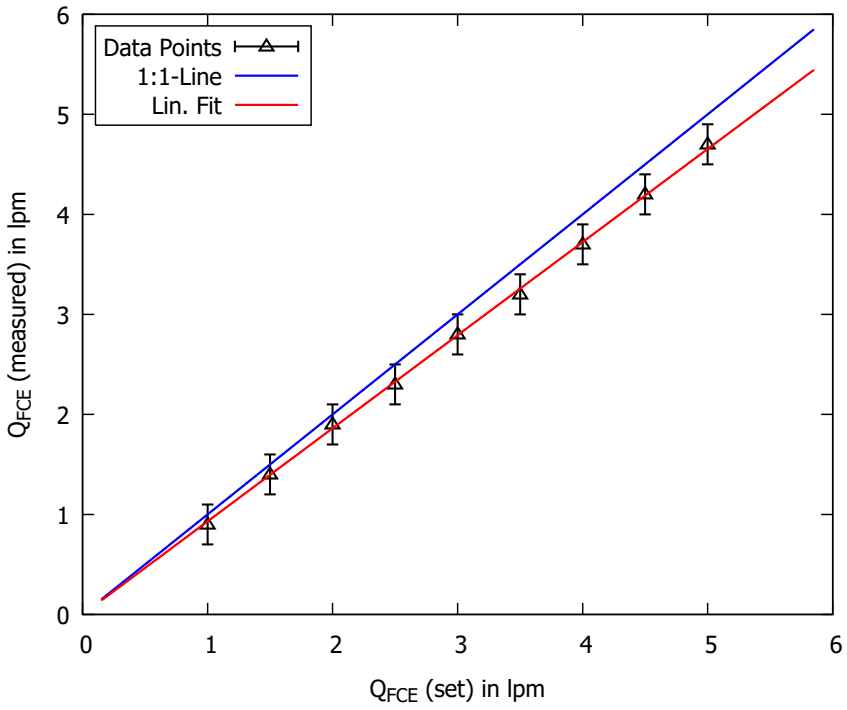

Figure 12: Flow calibration of the FCE. The red line shows a linear regression, while the blue line denotes the one-to-one ratio.

5.6.2 Linearity of the FCE

The second measurement regarding the FCE evaluates its linear behavior when moving up to high concentrations. This is especially important for the cutoff measurements of the CPC, as they need a stable reference instrument. The approach is the following: for any sample that yields a stable output, the corresponding concentration on the FCE and the CPC is recorded. To eliminate a possible drift and/or fluctuations in the concentration, the measurement runs for two minutes and then the mean value is taken. The results are shown in figure 13.

The sample consists of two high purity PET pellets, as their PNSDs are generally more stable over different temperatures than the commodity version. The voltage on the DMA is held at a constant value throughout the whole process, it corresponds to particles with a size of (11.9 ± 1.6) nm. To reach the desired different concentration values, the temperature is varied in the range of 228 - 238 °C.

For the uncertainty bars of the CPC, the standard deviation of the mean value is taken. In case of the FCE, these values are smaller than the data points in the plot, therefore they are not shown. A red line indicates a linear regression of the data and verifies that the trend is indeed linear. To illustrate a possible deviation, the one-to-one ratio between the two devices is indicated with a blue line.

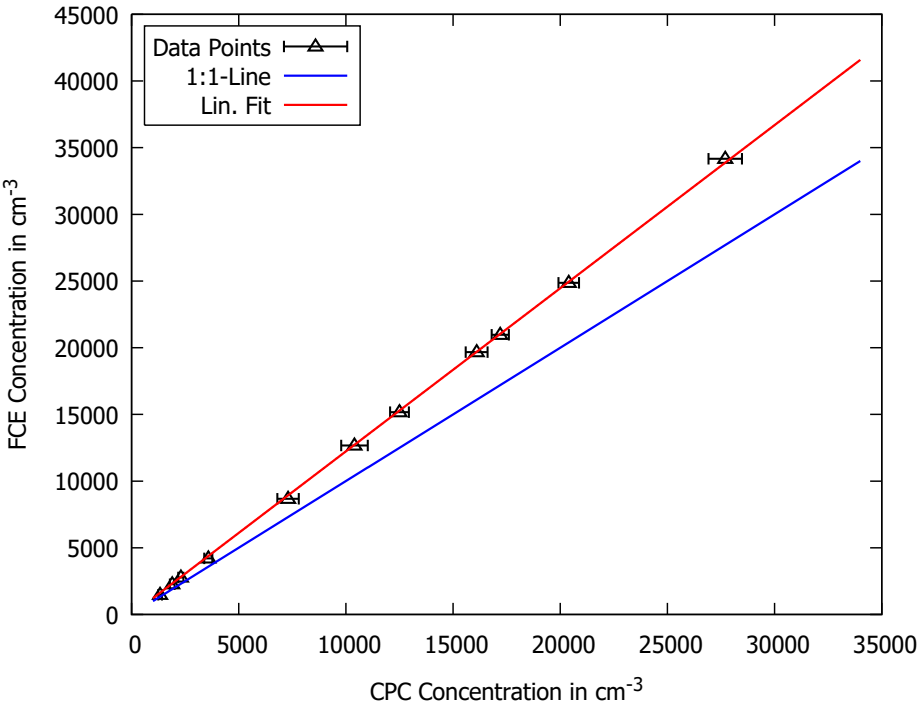

Figure 13: Linearity check of the FCE. The red line shows a linear regression of the data points. The blue line indicates the one-to-one ratio for reference.

By comparing the measured data with the ideal one-to-one line, it is visible that the offset of the concentration becomes significantly larger for higher concentrations. The approach for the cutoff measurements is therefore adapted in such a way, that the counts on the FCE always lie within the range of 3000 - 10 000 cm^{-3}. The lower border is necessary to ensure that the signal does not get lost in the background noise, and the upper limit ensures that the FCE offset does not get too big. The upper limit is in fact just an arbitrary value that stems from the challenge of the cutoff measurements. As it is difficult to obtain stable parameters for these measurements, the 10 000 cm^{-3} are simply an upper limit under which it is possible to vary all parameters and still obtain proper cutoff data.

Chapter 6

Results

This chapter summarizes the results from the PNSD measurements conducted under air and nitrogen as carrier gas, as well as the cutoff measurements of the CPC. For a proper and easier comparison, the plots in each subsection are all scaled to the same dimensions. The value of $\mathrm{d}N/\mathrm{d}\log(d_p)$ in cm^{-3} is presented in dependency of the equivalent mobility diameter d_p of the particles in nm.

The descriptive parameters of the obtained curves are all summarized in one table for each subsection. The tables contain values for the mode diameter d_m in nm, the geometric standard deviation σ_g, the peak concentration C_p in counts/cm^3 and the spread in the form of the full width at half maximum (FWHM) in nm of the PNSDs.

While C_p is a good measure for how strong the concentrations of the PNSDs react to different changes in the measuring conditions, it is important to mention that its value generally changes up to a factor of ten, when repeating the exact same measurements another day. The uncertainty of the FWHM can be estimated by the resolution of the DMA (13 %).

6.1 Measurements under Air

The following two subsections focus on the measurements conducted under air as carrier gas. All obtained PNSDs will be presented in six separate plots: three that show the behavior for the high purity version (PET) and three that highlight the behavior for the commodity version of PET (cPET).

Each plot displays three distinct curves that stem from a variation of either the setpoint temperature of the tube furnace, a change in the sample flow through the tube furnace or a different initial sample amount on the glass crucible. For a cleaner appearance, no error bars are displayed. However, the corresponding uncertainties stemming from the measuring devices are already discussed in the previous section *Possible Sources of Uncertainties* (5.4).

6.1.1 Results for High Purity PET (Air)

Figure 14 demonstrates the temperature dependency of the high purity PET plastic. The black curve shows the data for 260 °C, red indicates 250 °C and blue is the measurement for 240 °C. These temperatures are selected as they produce stable distributions. For lower values, the PNSDs become increasingly unstable over time until there is barely any distribution measurable for temperatures < 220 °C.

By changing the setpoint temperature of the tube furnace, it is possible to control the overall height of the PNSDs. In general, the trend holds that a higher temperature correlates with higher aerosol concentrations (see table 5). All temperature related measurements for the high purity PET are conducted with three pellets with a total mass of (77.3 ± 3.7) mg on the glass crucible and a flow rate of 1.6 lpm through the tube furnace.

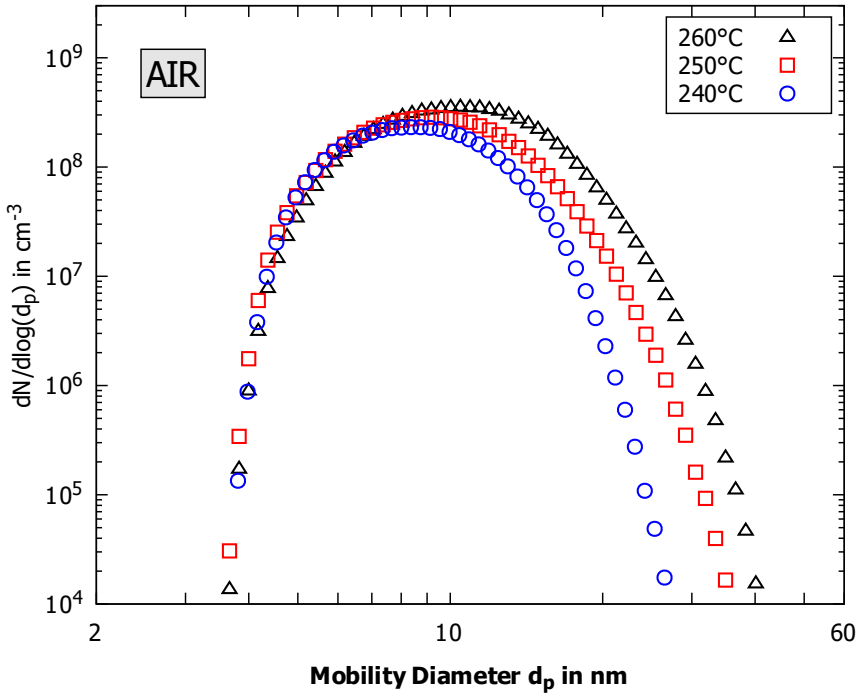

Figure 14: Measurements for PET plastic in air for various setpoint temperatures of the tube furnace. (3 pellets / $Q = 1.6$ lpm)

Another changing feature is the width of the distribution for bigger diameters. It follows a similar trend that higher temperatures yield a wider distribution. On the lower side of the diameters, all graphs fall down nearly identically - a strong indicator that the cutoff diameter of the CPC might play a vital role. This assumption will be discussed in section 6.4.

The position of the peak (mode diameter d_m) of the curves also shifts for higher temperatures towards larger values, when comparing the curve for 240 °C with $d_m = 8.4$ nm, one finds that the maximum shifts towards 10.5 nm for 260 °C.

In figure 15, the measurements of the variation in the flow rate are presented, as in the previous case they are conducted for three PET pellets. Again, from highest to lowest, the black, red and blue points present the data for 1.6 lpm, 1.2 lpm and 0.8 lpm. However, in this case, the data acquisition is more complicated than before.

For a proper measurement, the distribution needs to be stable. While stable curves can easily be found in the case of the variation of temperature, the measurements at different flow rates behave differently. If one temperature is stable for one specific value of the flow, it will not be stable for a different flow rate. This actually mirrors the expected behavior, as a higher flow through the tube furnace can be thought of as a cooling stream above the plastic sample. Therefore, the flow measurements result in three graphs that are complex to interpret, as each curve has a different temperature value, thus embodying also the temperature dependency as seen in the previous figure 14. This makes it hard to properly interpret the data and to find a significant trend in it. Table 5 summarizes the descriptive parameters of the curves where it is notable, how the FWHM of the PNSDs for a flow rate of 0.8 lpm changes from about 10 nm, as in the case of the other two curves, to approximately 5 nm. The peak concentration C_p is decreased by almost a factor of ten.

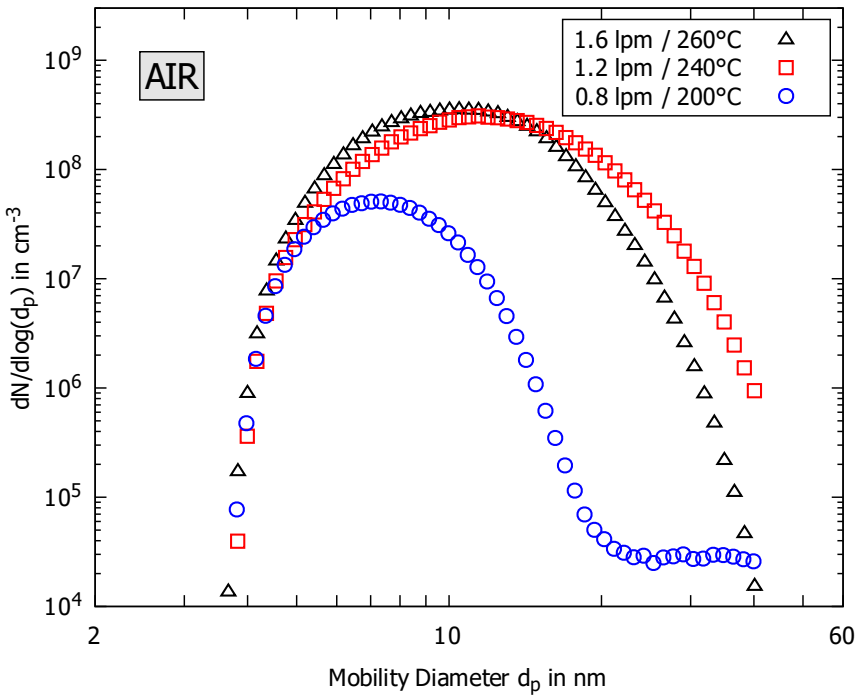

Figure 15: Measurements for PET plastic in air for different flow rates through the tube furnace. (3 pellets)

However, the common behavior of the steep decline at a diameter of about 4 nm for all three curves persists, again hinting at a cutoff effect of the CPC. Another occurring feature is the constant tail of the PNSD for a flow of 0.8 lpm. This effect is of unknown origin, it only appears in this excessive form in this specific configuration.

The third plot (fig. 16) shows the behavior for various initial sample amounts. For the high purity version, the PET plastic comes, as already discussed, in the form of tiny pellets. The measurements are displayed for 3 – 1 pellets. A peculiar detail is that the curves again exhibit a similar trend, as seen for the variation in temperature. While three pellets yield the highest concentration ($2.3 \cdot 10^8\,\mathrm{cm}^{-3}$) and widest distribution ($\sigma_g = 1,45$ / FWHM = 13.8 nm), all parameters decrease for lesser sample amount ($1.1 \cdot 10^8\,\mathrm{cm}^{-3}$ / $\sigma_g = 1,36$ / FWHM = 7.5 nm for 1 pellet).

These three measurements are conducted under the exact same settings each, namely a flow rate of $Q = 0.8$ lpm and a temperature of $T = 230\,^\circ$C. The settings are selected to keep a larger temperature offset towards the melting point of the plastic to avoid that the samples stick to the glass crucible for an easier change of the sample amount. Additionally, these selected values yield stable distributions for nitrogen gas as well as for air. This makes it possible to create a proper comparison of the differences of the PNSDs under a change of the carrier gas (see section 6.3).

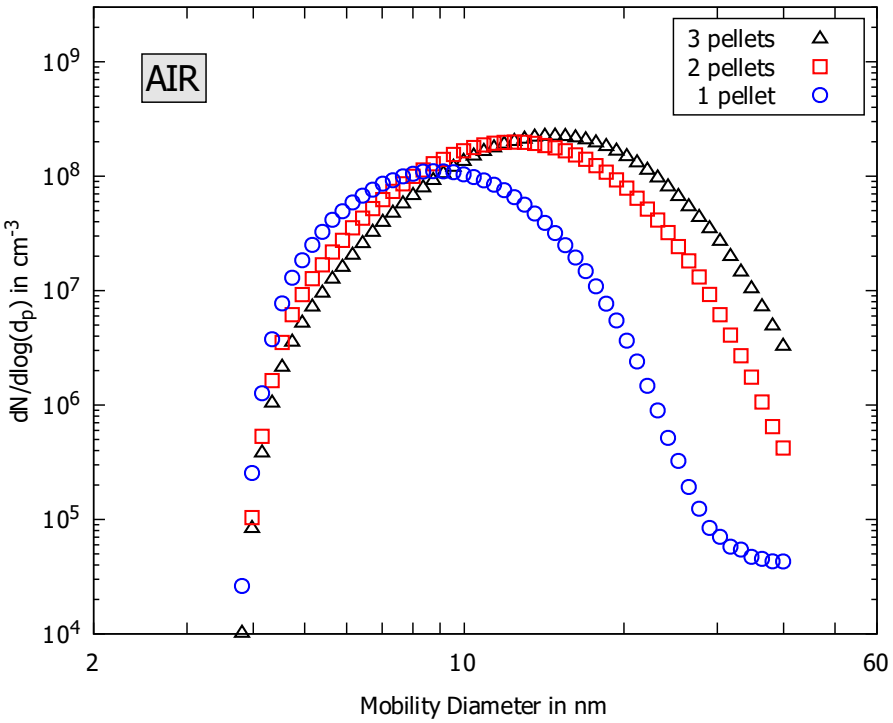

Figure 16: Measurements for PET plastic in air for different initial sample amounts on the glass crucible. ($T = 230\,^\circ$C / $Q = 0.8$ lpm)

For a proper description of all the plots above, table 5 collects all information. Among the mode and the geometric standard deviation, the peak concentration C_p is also given. While this parameter is generally less reproducible, it highlights how strong the concentrations of the PNSDs react to different applied changes.

Table 5: Summarized values for the PNSDs under air as carrier gas and for the high purity PET version. d_m denotes the mode diameter, σ_g the geometrical standard deviation, C_p the peak concentration at the position d_m and the FWHM denotes the spread of the respective distribution. The uncertainty of C_p is generally a factor of ten, while for the FWHM it is 13 %.

figure	parameter	d_m (nm)	σ_g (-)	C_p (cm^{-3})	FWHM (nm)
fig. 14	260 °C	10.5	1.40	3.6E+08	9.7
	250 °C	9.2	1.38	2.9E+08	8.3
	240 °C	8.4	1.34	2.3E+08	7.3
fig. 15	1.6 lpm	10.5	1.40	3.6E+08	9.7
	1.2 lpm	11.4	1.46	3.1E+08	11.3
	0.8 lpm	7.3	1.28	5.1E+07	5.2
fig. 16	3 pellets	14.8	1.45	2.3E+08	13.8
	2 pellets	12.4	1.42	2.0E+08	11.4
	1 pellet	8.7	1.36	1.1E+08	7.5

6.1.2 Results for Commodity cPET (Air)

This subsection focuses on a similar set of measurements, but this time with the commodity version (cPET) of the plastic. As in the previous subsection, the first plot (fig. 17) demonstrates the temperature dependency. The PNSDs are collected for the temperatures of 250 °C, 240 °C and 230 °C, indicated by black, red and blue.

As the cPET is harvested from a water bottle, the sample material is not on hand in the form of pellets, but rather in tiny, very thin snippets. Thus, it is necessary to use more of them on one glass crucible in order to get a sufficient amount of material. All the measurements shown in figure 17 are therefore conducted for five cPET pieces with a total mass of (49.0 ± 3.6) mg and a flow rate of $Q = 1.6$ lpm.

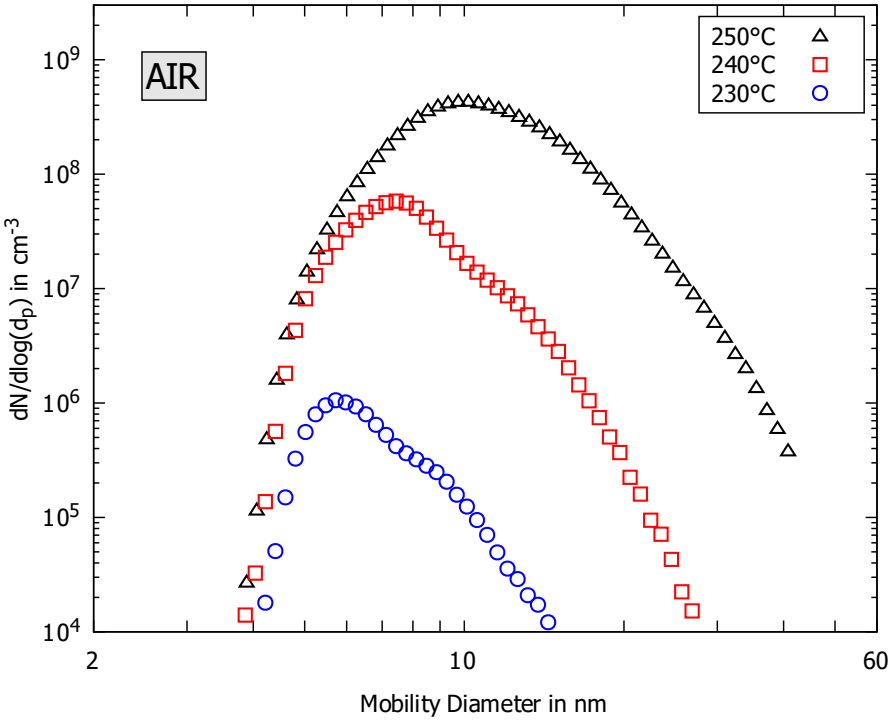

Figure 17: Measurements for cPET plastic in air for various setpoint temperatures of the tube furnace. (5 pieces / $Q = 1.6$ lpm)

As already found in the case for the high purity PET version, a higher setpoint temperature of the tube furnace yields not only higher concentrations, but also wider distributions. This trend is even more pronounced for cPET. Additionally, the shape of the PNSDs changes towards a more distinct peak when comparing it to the high purity version. For lower temperatures, a second, less defined bump forms on the side of larger particles, altering the form of the distribution. While the reason for this change in shape is yet unclear, it is totally possible that it stems from coagulation.

A quick estimate of the losses due to coagulation for a concentration of $C_p = 4.3 \cdot 10^8\,\mathrm{cm}^{-3}$ at a mode diameter of 10.2 nm, as in the case of the black curve for 250 °C, yields losses in the range of 20 - 25 %. This could definitely lead to a second peak that is superimposed in the wider distribution. That the shoulder itself is more visible for smaller concentrations could stem from the fact that it gradually gets lost in the broadening of the distribution for higher temperatures. After all, the change in the spread of the curves changes from a FWHM of 2.1 nm (blue curve at 230 °C) to 7.7 nm for the black curve at 250 °C.

Additionally, it is again observable that the position of the peak d_m steadily moves down from 10.2 nm to 7.4 nm and 5.7 nm when decreasing the setpoint temperature of the tube furnace (see table 6). During this change, the concentration strongly decreases by approximately a factor of 400.

The variation in the flow rate, as seen in figure 18, shows again a more complex behavior. Due to the necessity of a stable distribution, the temperature for the data collection of a flow of $Q = 1.6$ lpm has to be increased. Conveniently, it is possible to find a stable distribution at 230 °C for both other flows (1.2 lpm and 0.8 lpm). Again, all three measurements are conducted by using five cPET snippets.

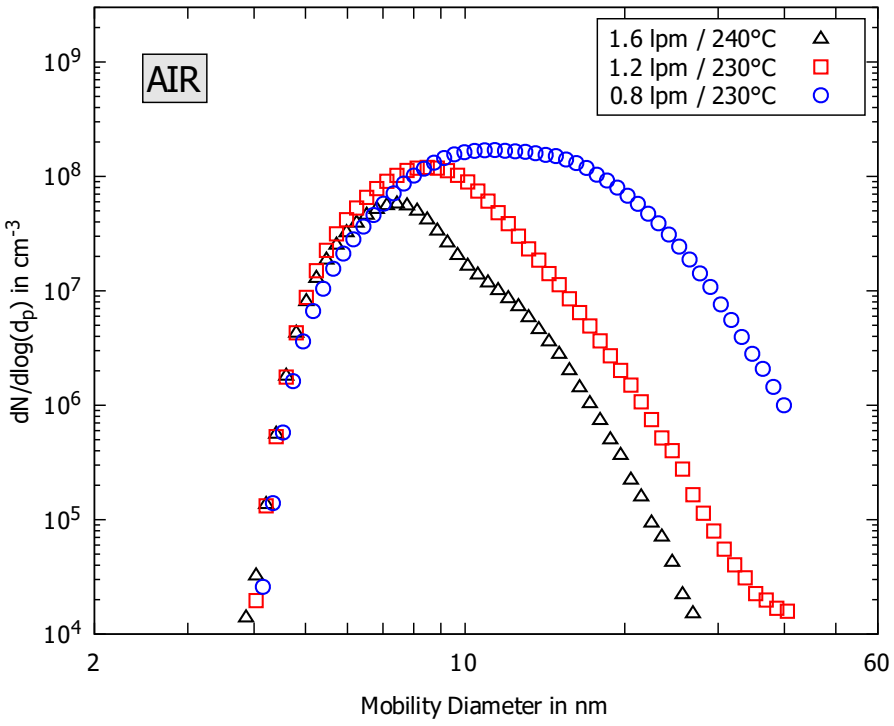

Figure 18: Measurements for cPET plastic in air for different flow rates through the tube furnace. (5 pieces)

Even though the temperatures do not coincide completely, they are similar enough to see a possible trend. When the flow is decreased, the PNSDs generally change towards higher concentrations (see table 6). While the data shows again a second bump in the distribution for the highest flow rate, it vanishes with the broadening of the distribution for lower values of the flow.

This seems to indicate an inverse trend as observed in the variation of the temperatures - which would make sense in a way that a lower air stream over the cPET sample for a stable temperature decreases its cooling effect. Thus, the tube furnace exerts stronger heating on the glass crucible, yielding an overall warmer sample and increasing the amount of particles in the carrier gas.

At last, figure 19 illustrates the behavior for a change in the initial sample amount of cPET plastic. As already mentioned, the snippets have a completely different shape and mass than the high purity PET pellets. Therefore, the amounts are changed to 7, 5 and 3 pieces (see section 5.5). However, the measurement conditions of $T = 230\,°\mathrm{C}$ and $Q = 0.8\,\mathrm{lpm}$ are maintained.

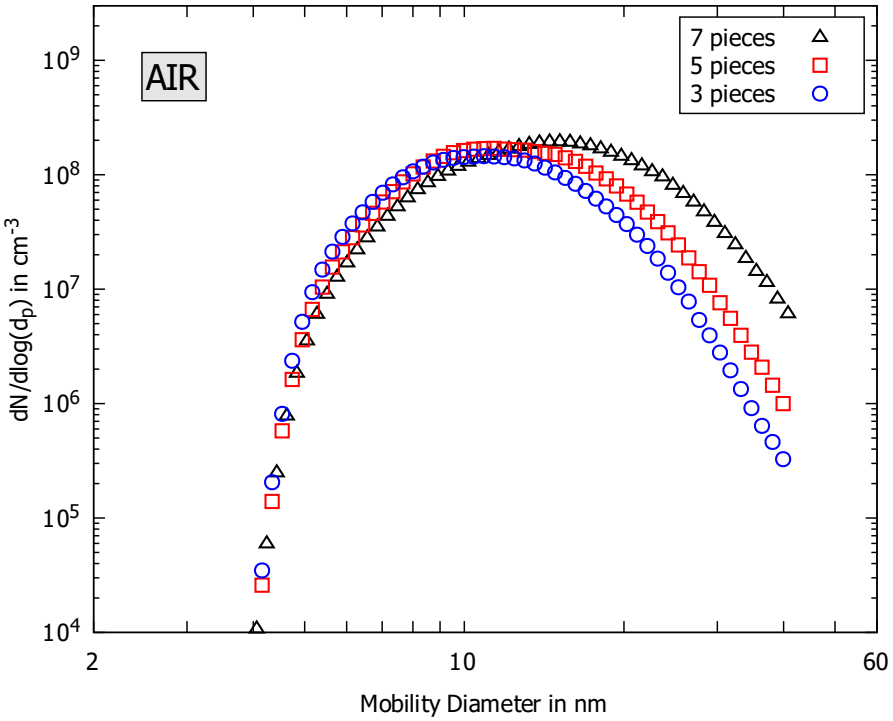

Figure 19: Measurements for cPET plastic in air for different initial sample amounts on the glass crucible. ($T = 230\,°\mathrm{C}$ / $Q = 0.8\,\mathrm{lpm}$)

While the observed trend is not as obvious as for the temperature measurements, there still seems to be a positive correlation between more sample material and higher concentrations - as well as a broadening of the distribution towards larger particle diameters.

Regarding the shift of the peak of the distribution, it is also again observable that it moves down from a mode diameter of 15.1 nm (black curve) to 11.4 nm (red curve) to 10.9 nm (blue curve). The FWHM spread of the PNSDs also decreases with a lower sample amount from 14.7 nm, as in the case of the black curve, to 9.9 nm for the lowest sample amount (blue curve). Table 6 summarizes the parameters of the obtained curves for this subsection.

A common characteristic of all three plots (17, 18, 19) is again the steep decline for all measurements at a particle size of about 4 nm. As this phenomenon already occurs throughout subsection 6.1.1, the cutoff diameter of the CPC seems to be a reasonable suspicion (section 6.4).

Table 6: Summarized values for the PNSDs under air as carrier gas and for the commodity cPET version. d_m denotes the mode diameter, σ_g the geometrical standard deviation, C_p the peak concentration at the position d_m and the FWHM denotes the spread of the respective distribution. The uncertainty of C_p is generally a factor of ten, while for the FWHM it is 13 %.

figure	parameter	d_m (nm)	σ_g (-)	C_p (cm^{-3})	FWHM (nm)
fig. 17	250 °C	10.2	1.36	4.3E+08	7.7
	240 °C	7.4	1.27	5.8E+07	3.4
	230 °C	5.7	1.27	1.1E+06	2.1
fig. 18	1.6 lpm	7.4	1.27	5.8E+07	3.4
	1.2 lpm	8.5	1.29	1.2E+08	5.1
	0.8 lpm	11.4	1.43	1.7E+08	11.7
fig. 19	7 pieces	15.1	1.47	2.0E+08	14.7
	5 pieces	11.4	1.43	1.7E+08	11.7
	3 pieces	10.9	1.41	1.5E+08	9.9

6.2 Measurements under Nitrogen

After the completed data acquisition for air as carrier gas, the exact same measurements are repeated, but this time with nitrogen gas (N_2). The measurements are again split up into two different subsections, one for the high purity PET version and one for the commodity (cPET) version.

Each plot consists of three distinct curves that highlight either a change of the setpoint temperature of the tube furnace, a variation of the flow rate through the tube furnace or a change of the initial plastic sample amount. As already in section 6.1, no error bars are displayed, as the plots would become too crowded. However, an in-depth discussion about the belonging errors that stem from the measuring devices, such as DMA and CPC, can be found in the section *Possible Sources of Uncertainties* (5.4).

As previously, the values of the mode diameter d_m in nm, the geometric standard deviation σ_g, the peak concentration C_p in counts/cm^3 and the spread in the form of the full width at half maximum (FWHM in nm) of the PNSDs are summarized for each subsection in one table.

6.2.1 Results for High Purity PET (N_2)

Figure 20 illustrates the temperature dependency for the high purity PET plastic under nitrogen as carrier gas. As already in the previous few subsections, the curves are displayed in three distinct colors, from black over red to blue, indicating the trend from a high value of the temperature towards a lower one.

In this case, the temperature steps have to be decreased from 10 °C to 5 °C. This comes from the fact that it is not possible to obtain a stable distribution for lower temperatures than 250 °C, thus yielding a lower boundary for the measurements. For the upper limiting temperature, it is not meaningful to increase further than 260 °C, as the melting point of the plastic is almost reached. Due to the lack of additional glass crucibles, the risk of burning the sample onto the glass could not be taken.

The results clearly indicate the trend that for higher temperatures, higher concentrations for the PNSDs are reached (see table 7). Another feature is that the width also broadens towards larger particle diameters for higher temperatures. For small particles, all curves fall steep down together, indicating a cutoff effect of the CPC around 4 nm (section 6.4). All three measurements are conducted under a flow rate of 1.6 lpm through the tube furnace with 3 high purity PET pellets (total mass of (77.3 ± 3.7) mg) on the glass crucible.

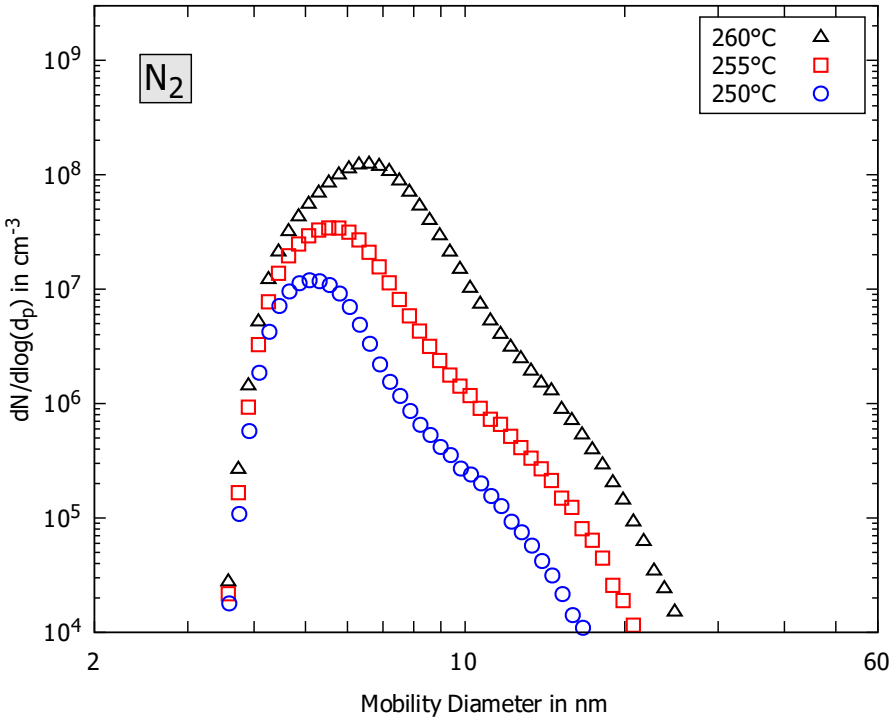

Figure 20: Measurements for PET plastic in nitrogen for various setpoint temperatures of the tube furnace. (3 pellets / $Q = 1.6\,\mathrm{lpm}$)

A remarkable detail is that the PNSDs obtain a different shape than in the case of the air measurement - they develop a shoulder on the side of larger particles (for a direct comparison of the air and the nitrogen carrier gas measurements see section 6.3). For the high purity version, this is a new behavior when comparing it to the measurements conducted under air. As discussed in subsection 6.1.2, this could possibly stem from coagulation of the particles, as the concentrations are rather high, like in the case of the black curve for 260 °C. At the position of the mode diameter (6.6 nm), the concentration reaches $1.3 \cdot 10^8\,\mathrm{cm}^{-3}$. As previously, the position of the PNSDs also continuously moves down from 6.6 nm (black curve at 260 °C) to 5.5 nm (red curve at 255 °C) to 5.1 nm (blue curve at 250 °C) when lowering the temperature.

The next measurements cover the change in the flow rate, as seen in figure 21. The challenge for the flow measurements is that by changing the flow, the distribution needs also a different temperature to become stable. This leads to a complex behavior of the measurements, where the temperature dependency possibly plays the major role compared to the flow dependency. It seems that the data is not sufficient to make a statement about the behavior of the distributions in this case, as particle production appears to be very sensitive to specific parameter changes. However, it is remarkable that the PNSD for a flow of 1.6 lpm again develops a shoulder towards larger particles. The reason behind this phenomenon is, as

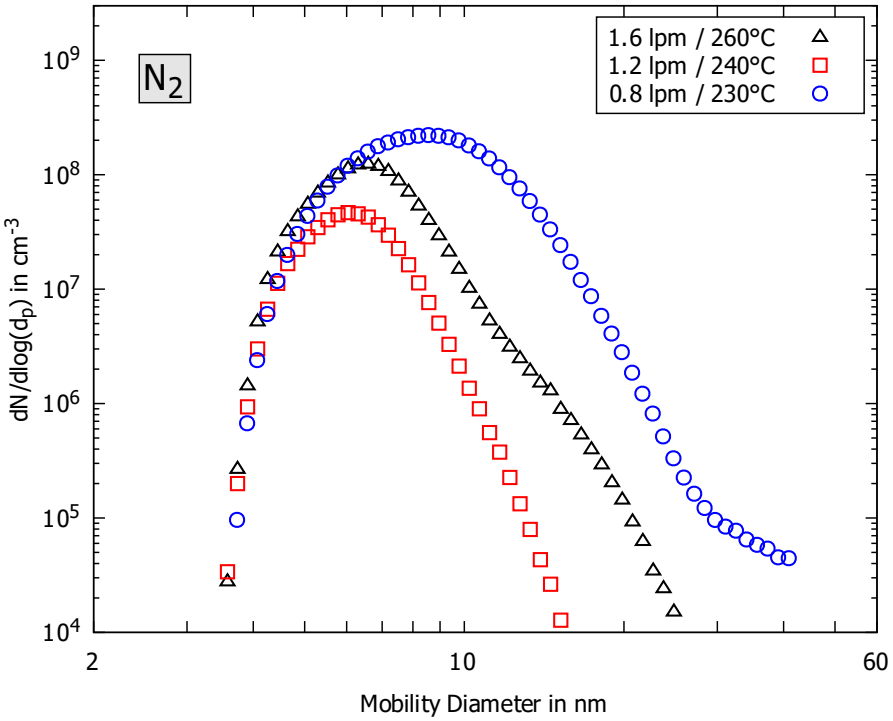

Figure 21: Measurements for PET plastic in nitrogen for different flow rates through the tube furnace. (3 pellets)

already discussed, probably coagulation due to the concentration ranges this measurements are dealing with. Interestingly, lowering the flow rate smooths out the PNSD, thus reducing the size of the shoulder.

The third plot (fig. 22) shows the measurements for a variation in the initial sample amount of PET plastic. All three curves are conducted under the exact same settings, namely $Q = 0.8\,\mathrm{lpm}$ and $T = 230\,^{\circ}\mathrm{C}$. While there is barely a difference noticeable in the PNSDs for three or two pellets, the data for one single plastic pellet yields fewer particles of almost a factor of ten at the peak. This indicates again the trend that a lower initial sample amount correlates with lower concentrations and a narrower PNSD on the side of the bigger particles.

By again comparing the position of d_m, one finds that a higher sample amount again positively correlates with a larger particle diameter for the peak position of the distribution: 8.6 nm for the black, 8.2 nm for the red curve (both with $\sigma_g = 1.32$) and 5.8 nm and $\sigma_g = 1.21$ for the blue curve. In addition, the FWHM spread of the blue curve is approximately half as wide, as for the other two measurements. A complete summary of the descriptive parameters for the curves of this subsection is presented in table 7.

One common feature that all three plots of this subsection share is the rapid decrease of the PNSDs on the lower diameter side. They all fall down nearly identically, hinting at a cutoff effect of the CPC (see section 6.4).

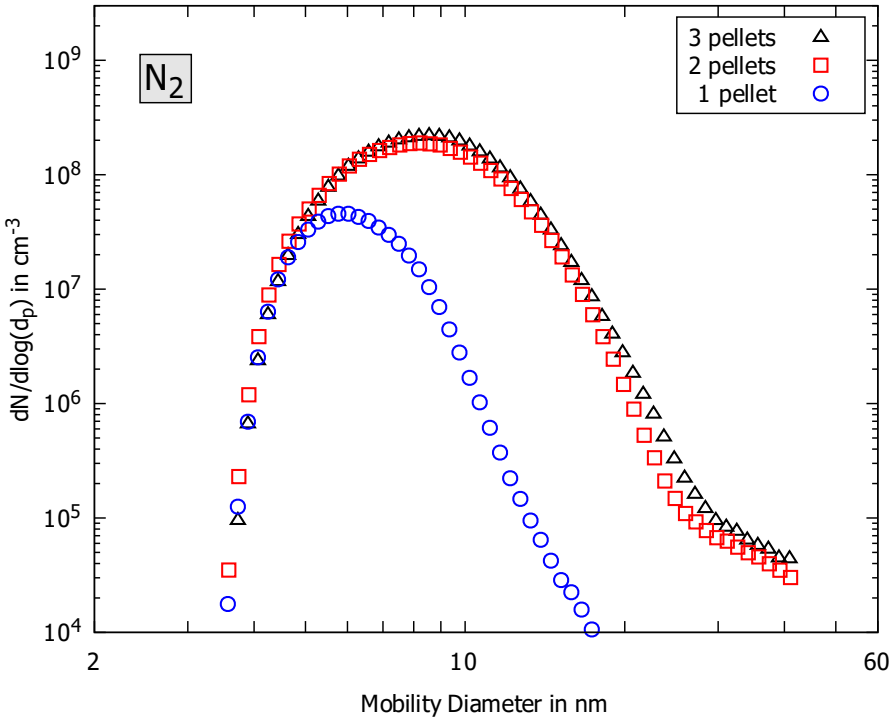

Figure 22: Measurements for PET plastic in nitrogen for different initial sample amounts on the glass crucible. ($T = 230\,°C$ / $Q = 0.8\,lpm$)

Table 7: Summarized values for the PNSDs under nitrogen as carrier gas and for the high purity PET version. d_m denotes the mode diameter, σ_g the geometrical standard deviation, C_p the peak concentration at the position d_m and the FWHM denotes the spread of the respective distribution. The uncertainty of C_p is generally a factor of ten, while for the FWHM it is 13 %.

figure	parameter	d_m (nm)	σ_g (-)	C_p (cm^{-3})	FWHM (nm)
fig. 20	260 °C	6.6	1.23	1.3E+08	3.0
	255 °C	5.5	1.22	3.4E+07	2.3
	250 °C	5.1	1.19	1.2E+07	1.9
fig. 21	1.6 lpm	6.6	1.23	1.3E+08	3.0
	1.2 lpm	6.0	1.20	4.7E+07	2.6
	0.8 lpm	8.6	1.32	2.2E+08	6.2
fig. 22	3 pellets	8.6	1.32	2.2E+08	6.2
	2 pellets	8.2	1.32	1.9E+08	6.0
	1 pellet	5.8	1.21	4.6E+07	3.1

6.2.2 Results for Commodity cPET (N_2)

The results of this subsection are again obtained similarly to the presented ones of the previous subsection. By using commodity cPET snippets, the temperature dependency under nitrogen gas is displayed in figure 23. This change is executed in steps of 5 °C for the same reasons as in the last subsection: for lower values than 250 °C, a stable distribution is not possible, while at 260 °C, the melting point of PET is almost reached.

The data clearly indicates the same trend as for high purity PET - an increase in temperature results in overall higher concentrations and a wider PNSD on the larger side of particle diameters. The measurements are conducted for five cPET pieces (total mass of (49.0 ± 3.6) mg) and a flow rate of 1.6 lpm through the tube furnace.

The peak position also changes from 7.5 nm for 260 °C down to 6.3 nm for 250 °C. By applying this change of temperature, the FWHM spread also decreases from 3.9 nm to 3 nm. As already in the measurements under air, the PNSDs again develop a shoulder for larger particle diameters - possibly stemming from coagulation due to the high concentrations of 10^7 - 10^8 cm^{-3} (see table 8).

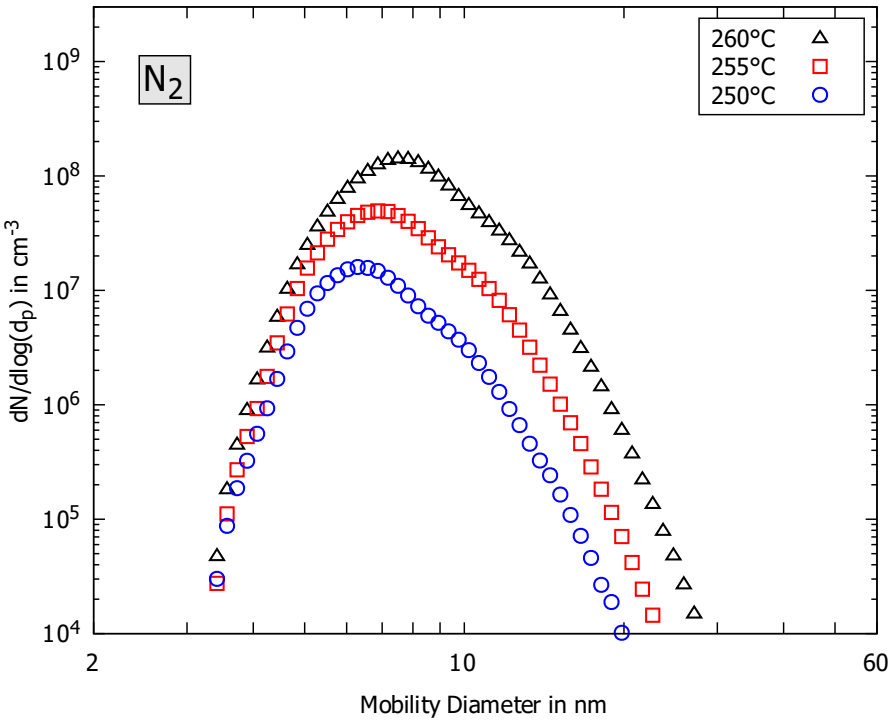

Figure 23: Measurements for cPET plastic in nitrogen for various setpoint temperatures of the tube furnace. (5 pieces / $Q = 1.6$ lpm)

The next steps are the measurements for a variation in the flow through the tube furnace. By using again five cPET snippets, PNSDs for three different flow configurations (0.8 lpm, 1.2 lpm and 1.6 lpm) are recorded. As a stable distribution is essential for a significant measurement, the temperature has to be changed adequately. In this case, no clear trend is evident after all the measurements are conducted for completely different temperatures, which probably introduce a trend coming from the initially shown temperature dependency.

The resulting curves are displayed in figure 24. In contrast to the other measurements, the heights and widths of the distributions are rather uniform with no significant trend, unlike in the case of the temperature dependency (see table 8). Interestingly, the black curve for a flow rate of 1.6 lpm has the narrowest width of all three displayed PNSDs with a FWHM of 3.9 nm. Despite these conditions, it can be clearly seen that the lowering of the flow rate smooths out the shoulder in the PNSD of 1.6 lpm. This has previously been observed for the variation of the flows for high purity PET, also conducted under nitrogen gas.

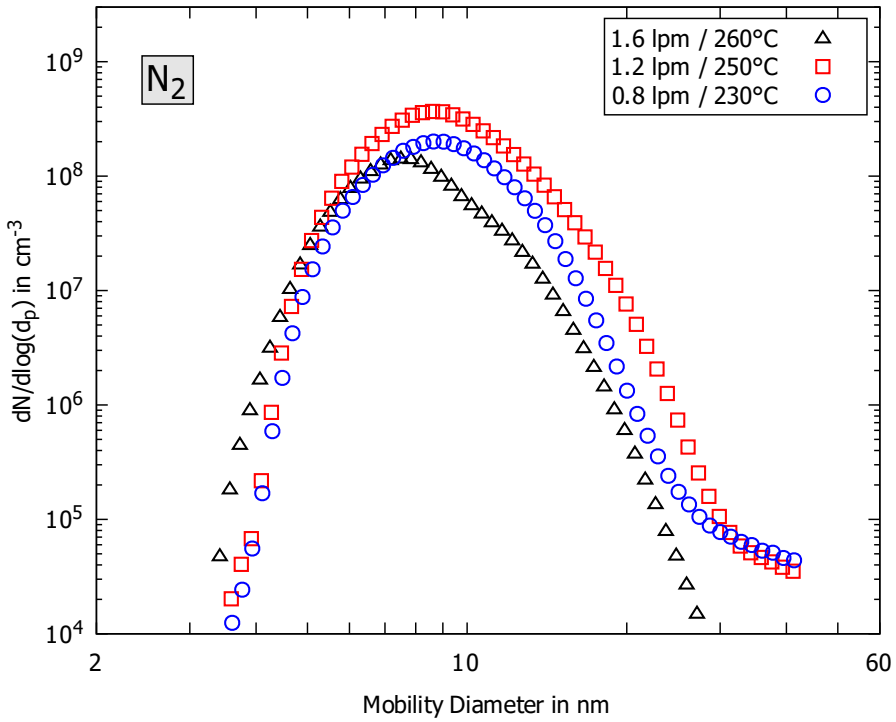

Figure 24: Measurements for cPET plastic in nitrogen for different flow rates through the tube furnace. (5 pieces)

The third plot (fig. 25) shows the dependency of the PNSDs with respect to the initial sample amount. To obtain this data, a fixed setpoint temperature of 230 °C is applied, together with a constant flow rate of 0.8 lpm. For the variation of the plastic amount, seven, five and three cPET snippets are used.

In comparison to the measurements under air as carrier gas, the sample amount dependency is far less pronounced. While the overall height of the peak does not change significantly in figure 25, a broadening of the distribution for seven cPET pieces is observed (FWHM = 9.9 nm). This happens again only on the side of larger particles. For five and three snippets, the FWHM has a value of 6.7 nm (red curve) and 8.2 nm (blue curve). Interestingly, for this specific case, the narrowest distribution is given by the intermediate sample amount. All the describing parameters of the curves of this chapter can be found in table 8.

By comparing the figures 23, 24 and 25, a steep decline of the PNSDs on the lower end can again be observed. In each plot it lies at roughly 4 nm - the possibility of a cutoff diameter from the CPC will be discussed in section 6.4.

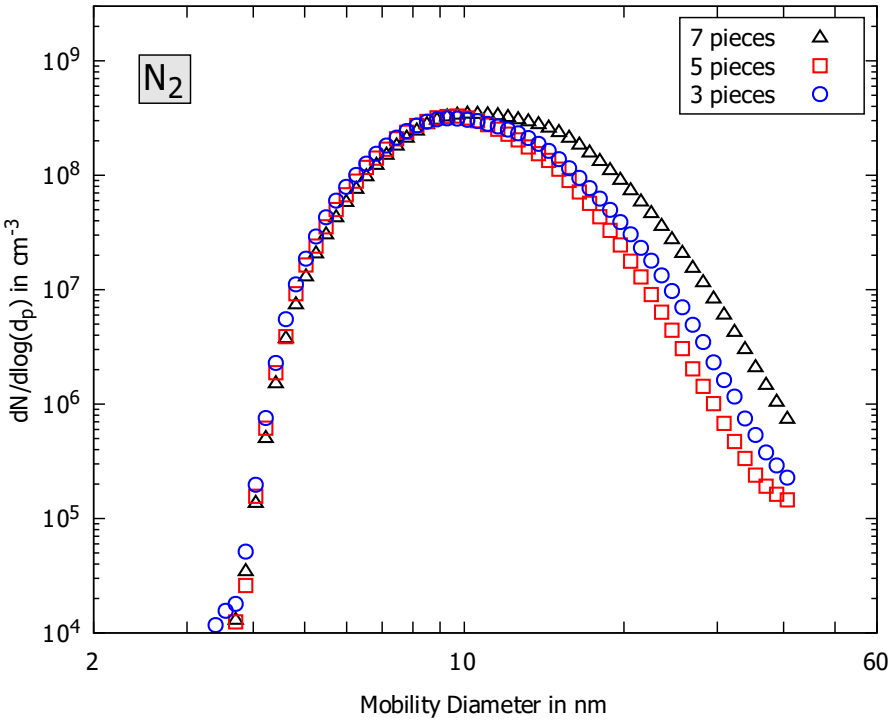

Figure 25: Measurements for cPET plastic in nitrogen for different initial sample amounts on the glass crucible. ($T = 230\,°C$ / $Q = 0.8\,lpm$)

Table 8: Summarized values for the PNSDs under nitrogen as carrier gas and for the commodity cPET version. d_m denotes the mode diameter, σ_g the geometrical standard deviation, C_p the peak concentration at the position d_m and the FWHM denotes the spread of the respective distribution. The uncertainty of C_p is generally a factor of ten, while for the FWHM it is 13 %.

figure	parameter	d_m (nm)	σ_g (-)	C_p (cm^{-3})	FWHM (nm)
fig. 23	260 °C	7.5	1.28	1.4E+08	3.9
	255 °C	6.9	1.27	4.9E+07	3.5
	250 °C	6.3	1.26	1.6E+07	3.0
fig. 24	1.6 lpm	7.5	1.28	1.4E+08	3.9
	1.2 lpm	8.6	1.30	3.7E+08	5.2
	0.8 lpm	8.6	1.28	2.0E+08	5.2
fig. 25	7 pieces	10.1	1.40	3.5E+08	9.9
	5 pieces	9.7	1.34	3.3E+08	6.7
	3 pieces	9.3	1.37	3.1E+08	8.2

6.3 Direct Comparison of Air and Nitrogen Measurements

To gain a better understanding of the resulting differences in the PNSDs when changing the carrier gas from air to nitrogen, four measurements under equal conditions are conducted. To accomplish this task, it is necessary to find settings under which all distributions are stable.

One possible point is given at a flow rate of 0.8 lpm and a temperature of 230 °C. These two parameters are fixed throughout the whole measurement procedure. For an easier comparison, the sample amount of the high purity PET also equals the amount of cPET within the associated uncertainties. This is accomplished by using two PET pellets and five cPET pieces:

$$M_{PET} = (51.5 \pm 2.5)\,\text{mg} \qquad \rightarrow \text{ 2 PET pellets}$$
$$M_{cPET} = (49.0 \pm 3.6)\,\text{mg} \qquad \rightarrow \text{ 5 cPET pieces}$$

In figure 26, the corresponding curves are displayed. While the black and the red data points present the data for air, blue and green indicate the measurements for nitrogen as carrier gas. Notice that the data collection for one type of carrier gas (air/nitrogen) is always done during one day, thus the four curves do not stem from the exact same day.

The two measurements under air yield similar curves, with no significant deviation from each other. They span from the steep onset, approximately at 4 nm, all towards the end of the measuring range of the DMA, namely 40 nm.

In nitrogen, however, the two curves exhibit a different behavior. While the high purity PET version has a peak at a mode diameter of 6.9 nm ($\sigma_g = 1.28$), the commodity plastic shifts its peak towards larger particles (9.0 nm / $\sigma_g = 1.32$). In addition, its distribution spans wider towards the larger particle end: FWHM of 6.4 nm for cPET vs. 5.0 nm for PET. Additionally, the peak concentration C_p of cPET is enhanced by a factor of two.

By comparing the nitrogen curves to the measurements under air (d_m(PET) = 12.4 nm and d_m(cPET) = 11.4 nm, a significant phenomenon is that the position of the peak of the PNSDs shifts towards lower particle diameters. This holds for the high purity as well as for the commodity version. Additionally, the concentration of lower sized particles in the range of about 4 nm up to 10 nm is enhanced up to a factor of ten. The corresponding values for the mode d_m, the geometrical standard deviation σ_g, the peak concentration C_p and the FWHM spread of the PNSDs can be found in table 9.

In air, an increased amount of particles > 8 nm can be detected for the high purity plastic version. For cPET under air, the particle concentration is enhanced above 12 nm. Despite their differences, all curves have one common characteristic - the steep decline of the PNSD around particles with diameters of 4 nm.

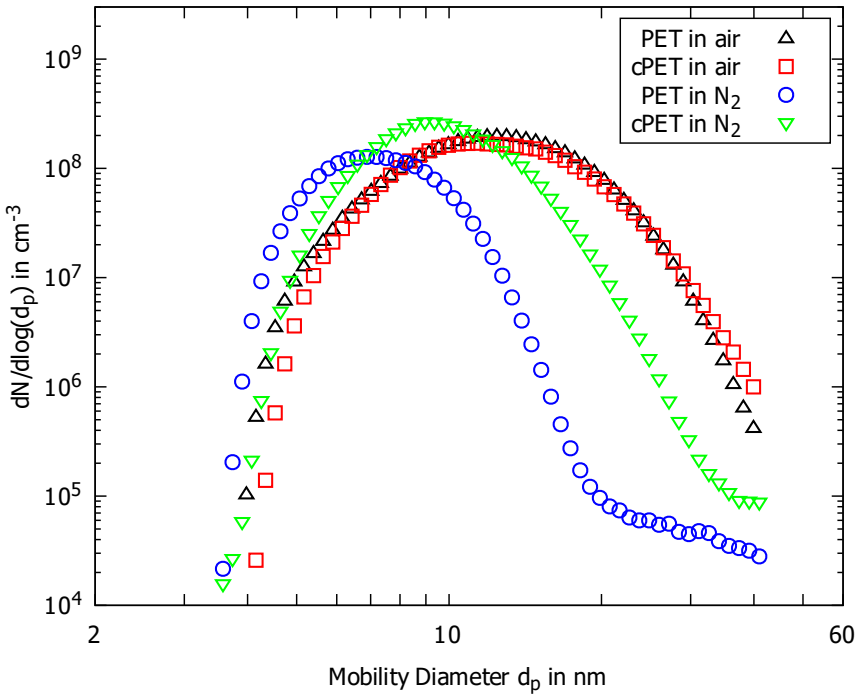

Figure 26: Comparison measurements for high purity PET and commodity cPET under different carrier gases. The setpoint temperature of the tube furnace is held constantly at 230 °C at a flow rate of 0.8 lpm. The masses of the plastic amount are fixed throughout the whole measurement. The black and the red data points represent the results for air, while the blue and green points mark the obtained values for nitrogen gas.

Table 9: Summarized values for the PNSDs under air/nitrogen as carrier gas and for the PET/cPET samples. d_m denotes the mode diameter, σ_g the geometrical standard deviation, C_p the peak concentration at the position d_m and the FWHM denotes the spread of the respective distribution. The uncertainty of C_p is generally a factor of ten, while for the FWHM it is 13 %.

carrier gas	plastic type	d_m (nm)	σ_g (-)	C_p (cm^{-3})	FWHM (nm)
air	PET	12.4	1.42	2.0E+08	11.4
air	cPET	11.4	1.43	1.7E+08	11.7
N_2	PET	6.9	1.28	1.3E+08	5.0
N_2	cPET	9.0	1.32	2.6E+08	6.4

6.4 Cutoff Measurements of the CPC

A common way to determine the lower measuring boundary of a CPC is to characterize it by its cutoff diameter. The basic principles behind the cutoff diameter are summarized in subsection 4.4.1. In the following two subsections, the cutoff diameter will be evaluated for two different configurations of the nano water-based CPC (model TSI 3788).

The first one will use air as carrier gas and present the results for both, high purity and commodity PET plastic. In contrast to them, the second subsection focuses on the same measurements conducted under nitrogen gas. For each measurement, a Wiedensohler fit function is applied to the data points, yielding insights to the specific value of the cutoff diameter for each plastic type.

6.4.1 Cutoff Diameter for Air

In figure 27, the results for the cutoff curve under air are presented. While the black data points show the measurements for the high purity PET plastic, the red points depict the results for the commodity version (cPET). The two fit functions, drawn with the respective color, show a Wiedensohler fit that is used to properly determine the value of the cutoff diameter. The base values for the plot are summarized together with their belonging uncertainties in table B.1 in the appendix.

An ideal cutoff curve would rise up steep and then approach a value of one - indicating a counting efficiency of 100 %. However, a peculiar detail in the fitted data is that the ratio η between CPC and FCE forms a plateau η_{max} at a value of about 80 % for both kinds of plastic. While it looks like the high purity plastic version has a slightly lower plateau value, both heights coincide within their associated uncertainties, see table 10. The belonging uncertainties for η_{max} are not coming from the fit, they are obtained by a maximum error estimation based on the measurement data.

Table 10: The CPC cutoff diameters $d_{p,50}$ for air. The parameter η_{max} characterizes the height of the plateau, obtained by the Wiedensohler fit function. The uncertainty for both cutoff diameters comes from [50], where the geometrical standard deviation is estimated for the corresponding particle size range.

Plastic	$d_{p,50}$	η_{max}
PET	(3.81 ± 0.20) nm	(75.1 ± 9.6) %
cPET	(3.72 ± 0.20) nm	(78.3 ± 8.5) %

For the correct calculation of the ratio η, the background noise of the FCE has to be removed prior to the calculation. In theory, the same applies to the concentration of the CPC, but as its own background noise is in the range of one or two counts/cm^3, it can be neglected. However, this approach can not be explanatory for the offset of the plateau of about 20 %. One reason for this phenomenon is that the measuring devices are completely different equipments. While the FCE has a rather straight forward measuring principle, the CPC uses a lot of tubings to direct the aerosol into the desired chambers. This unavoidable circumstances probably form the main contribution to this mismatch.

The desired cutoff diameters $d_{p,50}$ are obtained by calculations using the Wiedensohler fit. Their values are also displayed in table 10. The belonging uncertainties stem from [50] where the geometric standard deviation for the corresponding CPC in the respective size range is depicted in a graph. Even if the two curves in figure 27 seem to have a slightly different slope, there is no evidence in the values that the cutoff diameters are different under air for PET or cPET plastic.

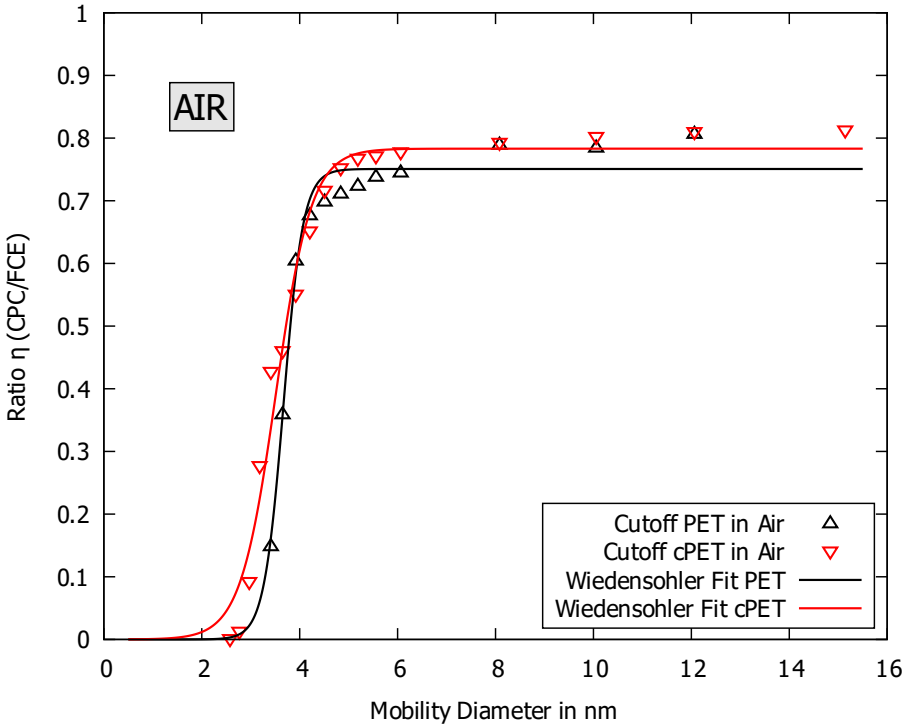

Figure 27: Cutoff curve of the CPC (model 3788) for air as carrier gas. The black data points show the measurements for high purity PET, the red ones for the commodity cPET version. The lines with the corresponding colors show the Wiedensohler fit functions.

The majority of the measuring points are conducted between approximately 2 and 6 nm, this comes from the initial suspicion that the cutoff diameter would lie at approximately 4 nm. The measurement points for larger particle diameters are then taken to examine the position and shape of the plateau. As can be seen from the fit of the high purity PET, the upper part, where the function reaches its plateau, is smeared out around the elbow of the curve. This effect is possibly stemming from diffusion within the CPC.

On the left side of the cutoff curve, the measurements are limited to a particle diameter size of about 2.5 nm. This limitation comes from the occurrence of charger ions in the measurements of the FCE in this size range. As they restrain the data evaluation, no more measuring points are taken. Conveniently, the concentration of the CPC is already shrunken down to almost zero, thus leaving no need for further data points.

As mentioned in the previous subsections of *Measurements under Air* (6.1), the PNSDs all shrink down at a similar lower boundary. This happens to be exactly the position of the cutoff diameter, thus limiting the lower side of the measurements. While it does not allow to properly examine the decline of the PNSDs on the lower side, the overall shape and the position of the peak can both be investigated without problems.

6.4.2 Cutoff Diameter for Nitrogen

The same measurements as in the previous subsection are conducted again, but this time with nitrogen as carrier gas. Figure 28 shows the results - the black data points display the high purity PET and the red points the commodity cPET measurements. The Wiedensohler fit functions are drawn with the corresponding colors. All the base values with their corresponding uncertainties can be fond in the appendix in table C.1.

To recap, an ideal cutoff curve would converge towards a value of 100 %. However, the obtained values for the position of the plateau (η_{max}) are lower, as shown in table 11. The uncertainties for η_{max} are again coming from a maximum error estimation. Within these uncertainties, it is again not possible to determine any discrepancy in the height for PET or cPET. As shown in figure 28, the same goes also for the values of the cutoff diameters $d_{p,50}$. After all, the black and red curve are almost identical in their slope and the position of their increase. Their values are also displayed in table 11. For the cutoff diameters, the uncertainty comes again from the corresponding geometrical standard deviation, as shown in [50].

Table 11: The CPC cutoff diameters $d_{p,50}$ for nitrogen gas. The parameter η_{max} characterizes the height of the plateau, obtained by the Wiedensohler fit function. The uncertainty for both cutoff diameters comes from [50], where the geometrical standard deviation is estimated for the corresponding particle size range.

Plastic	$d_{p,50}$	η_{max}
PET	(4.43 ± 0.23) nm	(82.3 ± 30.0) %
cPET	(4.54 ± 0.23) nm	(79.4 ± 20.0) %

Similar to the values of $d_{p,50}$ under air, the cutoff diameters lie so close together that there is no distinction possible between the two plastics. When comparing them to the previously obtained values, however, a change towards slightly larger cutoff diameters under nitrogen is observed. This change lies in the range of 0.7 - 0.8 nm and is not covered by the estimated uncertainties of $d_{p,50}$, therefore it might be hinting at a possible difference in the chemical composition of the aerosol particles (see chapter 7).

Regarding the lower end of the curve, the data points spread down to approximately 2.5 nm, as this is the range where the charger ions from the FCE start to appear, thus limiting the possibility of a proper data evaluation. For particle diameters larger than 6 nm, a few more data points are collected to properly map out the shape and position of the plateau.

As mentioned in the previous subsections of *Measurements under Nitrogen* (6.2), the PNSDs all shrink down at a similar lower boundary in the region around 4 nm. As clarified by this subsection, this likely happens due to the cutoff effect of the CPC. After all, the FCE indicated with a few data points spanning below the threshold of the cutoff diameter that the onset of the PNSDs possibly lies in this size region. But due to the occurrence of charger ions that alter the signal of the FCE in this size range, these measurements do not represent any significant data points for further analysis. While these factors do not allow a proper examination of the decline of the PNSDs on the lower side, the overall shape and the position of the peak can both be investigated without any issues.

To put the obtained cutoff values of the CPC model TSI 3788 into perspective, one can compare them to the values given by [51]: for strongly hydrophilic particles, the cutoff diameter reaches as low as 2.2 nm (NaCl - table salt) and for candle-generated particles, it lies at around 3.8 nm. The latter seems to be in good agreement with the obtained value of this thesis under air. In addition, [52] states that $d_{p,50}$ for silver nanoparticles has a value of approximately 3.2 nm - an indicator, that the cutoff diameters under nitrogen gas have a rather high value in comparison to air.

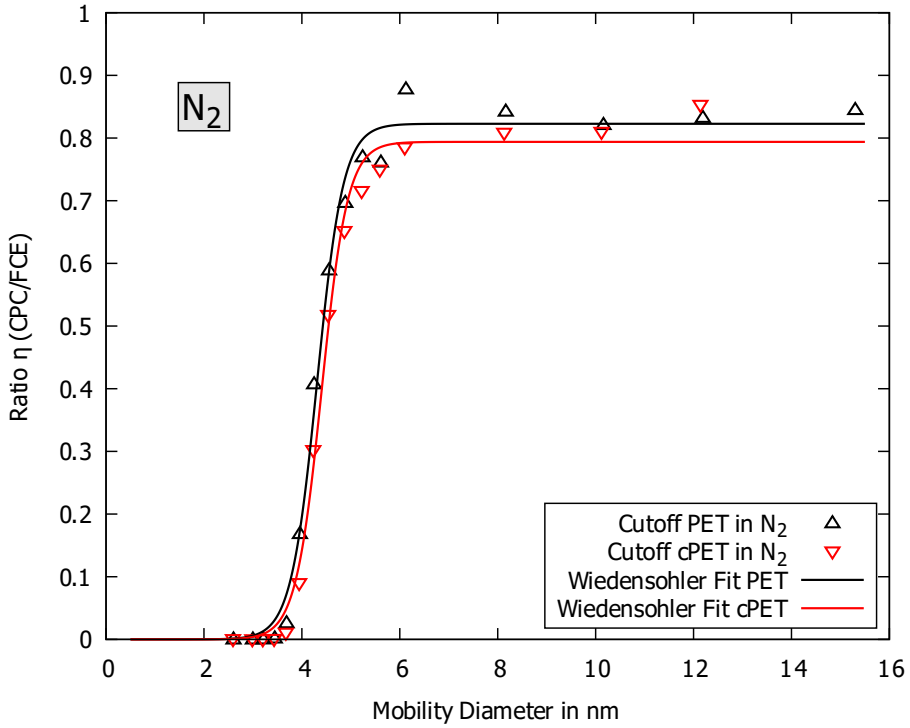

Figure 28: Cutoff curve of the CPC (model 3788) for nitrogen as carrier gas. The black data points show the measurements for high purity PET, the red ones for the commodity cPET version. The lines with the corresponding colors show the Wiedensohler fit functions.

6.5 Discoloration of the Plastic Samples

In addition to the PNSD measurements, the discoloration of the plastics is also monitored. The starting condition is shown in figure 29(a), where the fresh PET pellets (left) and cPET pieces (right) are shown. The PET samples are initially white, opaque and of cylindrical form. Their length is approximately 4 mm, while their diameter equals roughly 3 mm. In contrast to them, the cPET samples are colorless and transparent. They come in the form of flat circles, as they are punched out of a water bottle with a hole puncher. Their diameter equals 6 mm while their thickness is below half a millimeter.

During the measurements regarding the PNSDs and the cutoff curves, the samples undergo a significant change in color. This is shown in figure 29(b). Despite temperatures up to 260 °C during the measurements, the plastics do not melt into the glass crucible. Some of them stick slightly to the glass, but with a pair of tweezers it is possible to remove them completely. The PET pellets keep their overall form and change to a dark brown hue. The cPET pieces however shrink in size into an oval shape and their thickness increases to almost a millimeter. In addition, their transparency disappears, and they reach an opaque yellow/brown shade of color.

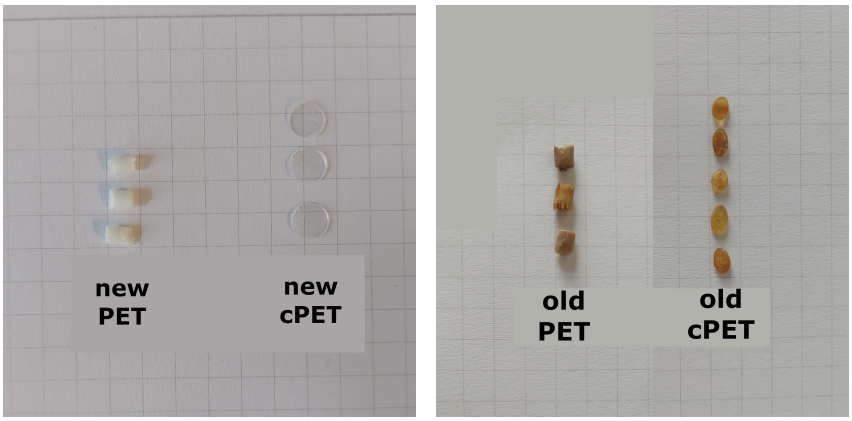

(a) initial samples (b) final samples

Figure 29: PET and cPET samples before and after multiple reheatings to different temperatures for the cutoff measurements under air. For reference, the background grid is 5 mm in width. (a) Initial samples: high purity PET (left) and commodity cPET (right). The PET pellets are of white color and opaque, while the cPET pieces are transparent and colorless. (b) Final samples: high purity PET (left) and commodity cPET (right). The PET pellets turn their color into a dark brown, while the cPET pieces shrink in size and change into an oval shape. Their thickness increases and they turn from transparent to an opaque yellow/brown hue.

The process of discoloration is monitored two times: once for a single heat up of about 40 min under air/nitrogen and the second time for multiple reheatings (40, 100, 100 min) with cooling phases in between. The results of the first part are shown in figure 30. The two pictures in the first line show the resulting color of the high purity PET plastic under air (fig. 30(a)) and under nitrogen as carrier gas (fig. 30(b)).

When comparing them to the initial sample in figure 29(a), a noticeable detail is that the pellets under nitrogen gas do not exhibit any change in color. Apart from the fact that they flatten slightly due to the heat, they show no other change at all. In contrast to them, the pellets under air change their color to a slight yellow/brown hue.

The second row of figure 30 shows pictures of the commodity plastics, again after one single heating under air and nitrogen (figs. 30(c) and 30(d)). The first obvious fact is the significant change in size. No matter of the carrier gas, the commodity plastics shrink into an oval form with a length of approximately three to four millimeters. Additionally, their thickness increases to almost one millimeter.

For air (fig. 30(c)), they lose their transparency and change towards an opaque white/yellow color tone. In nitrogen gas, however (fig. 30(d)), there occur two distinct scenarios: either they keep their transparency and only change their shape (top two pieces), or they melt into

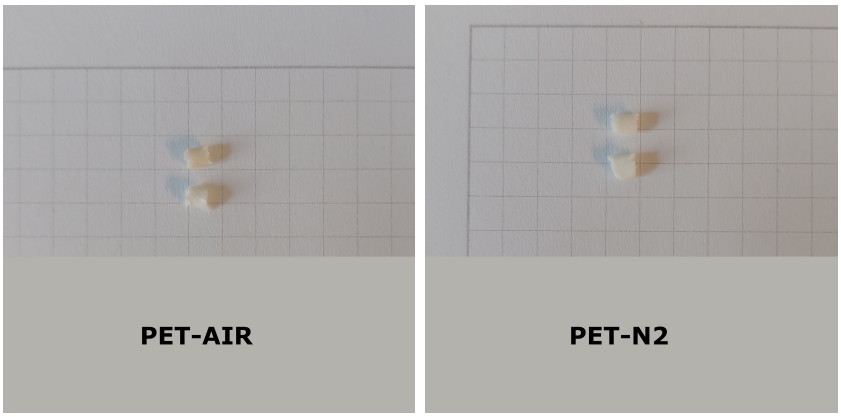

(a) PET in air (b) PET in nitrogen

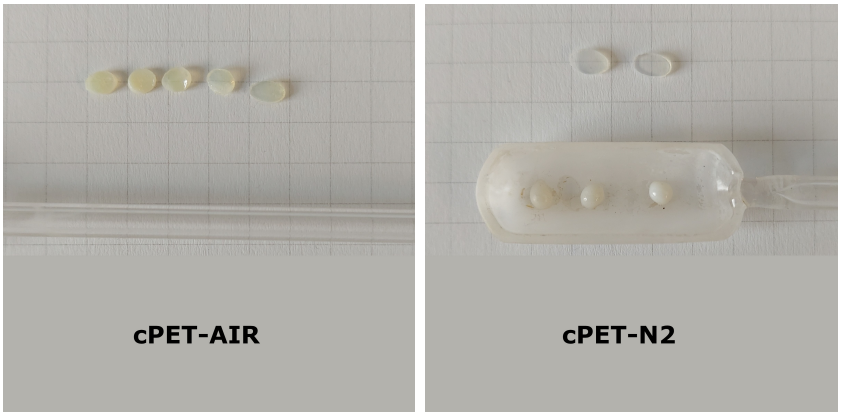

(c) cPET in air (d) cPET in nitrogen

Figure 30: One single heat up (40 min) of different samples under air and nitrogen as the carrier gas. For reference, the background grid is 5 mm in width. (a) High purity PET pellets change their color in air to a slight yellow/brown hue. (b) High purity PET pellets in nitrogen gas keep their initial white color. (c) cPET pieces change their shape in air, they shrink to an oval form and gain an opaque white/yellow hue. (d) cPET pieces change their shape in two different ways in nitrogen. They either shrink to an oval form and stay transparent, or they melt into a round drop of plastic that becomes opaque and gains a pure white color.

tiny round drops of plastic (lower three pieces on the glass crucible). In the second case, they turn pure white and melt into small plastic droplets of around 3 mm in diameter. They completely stick to the glass crucible, thus it is no longer possible to extract them from it.

Regarding figure 30(d), it is important to mention that two pieces of the samples were added a little later: to make sure that no air is involved in the discoloration process when using nitrogen as the carrier gas, the sample needs to cool down to a low temperature, before opening the measurement circuit to switch the sample. However, as the glass crucible could not fit all five cPET pieces at once on it, the first three were heated for a short time and

then the last two were added quickly, thus opening the circuit for a few seconds and letting air stream in. This probably led to the change in color of the three pieces shown on the glass crucible. The two snippets that were inserted later, however, stayed transparent. We will see that their behavior is a proper description of the actual change under nitrogen gas - this point will be addressed later in this section in more detail. Due to this fact, the measurement was not repeated a second time.

The next measurement is the observation of a possible gradual color change for multiple reheatings of both plastic samples in air. Due to a lack of glass crucibles, both the high purity and the commodity version are heated up simultaneously on one single glass crucible. In figure 31 the process is depicted over the course of three consecutive heatings for air as carrier gas.

The first picture (fig. 31(a)) shows the initial starting conditions. To recap, the high purity PET pellets are clean white, while the commodity cPET pieces are transparent and appear in a circular shape. The dark brown spot in the background is an old discoloration of the glass. To make sure that it has no impact on the measuring procedure, the glass crucible is tested for any contamination in the tube furnace. However, up to a temperature of 300 °C, which is much higher than the measurements go, no counts are detected on the CPC. It is therefore assumed that it will have no further effect on the following results.

After the first heating and cooling cycle, picture 31(b) is taken. The high purity PET pellets have melted into round droplets and start already to significantly change their color towards a brown hue. The initially transparent cPET pieces start to melt away and become opaque. Their look becomes similar to translucent glass, with a slight yellowish tint. The fact that all the plastic samples actually melt onto the glass crucible will be discussed later.

The result of the second heating/cooling cycle is shown in figure 31(c). One can see that the two pellets in the lower half of the picture darken further, while the commodity pieces gradually lose their transparency, melt away further and gain a significant yellow tint.
In the fourth picture (fig. 31(d)), the end result after the finished third heating and cooling cycle is shown. The high purity PET pellets darken a little more, while one of them gains a significantly darker border. The commodity plastic pieces change now to completely opaque and gain a strong yellow/brown color. At a few positions, the melted pieces even crack after the cooling, indicating that the material gets brittle in its solidified form.

In summary, figure 31 shows that the trend of the discoloration in air significantly increases with the number of reheatings. The total time the plastic is actually held on the high temperature, however, plays a vanishing role, as seen in figure 30.

In contrast, the subsequent measurements under nitrogen as carrier gas yield an opposing outcome. For a clearer result, these measurements are conducted with a different glass crucible for each plastic type. The resulting pictures are shown in figure 32. The measurements

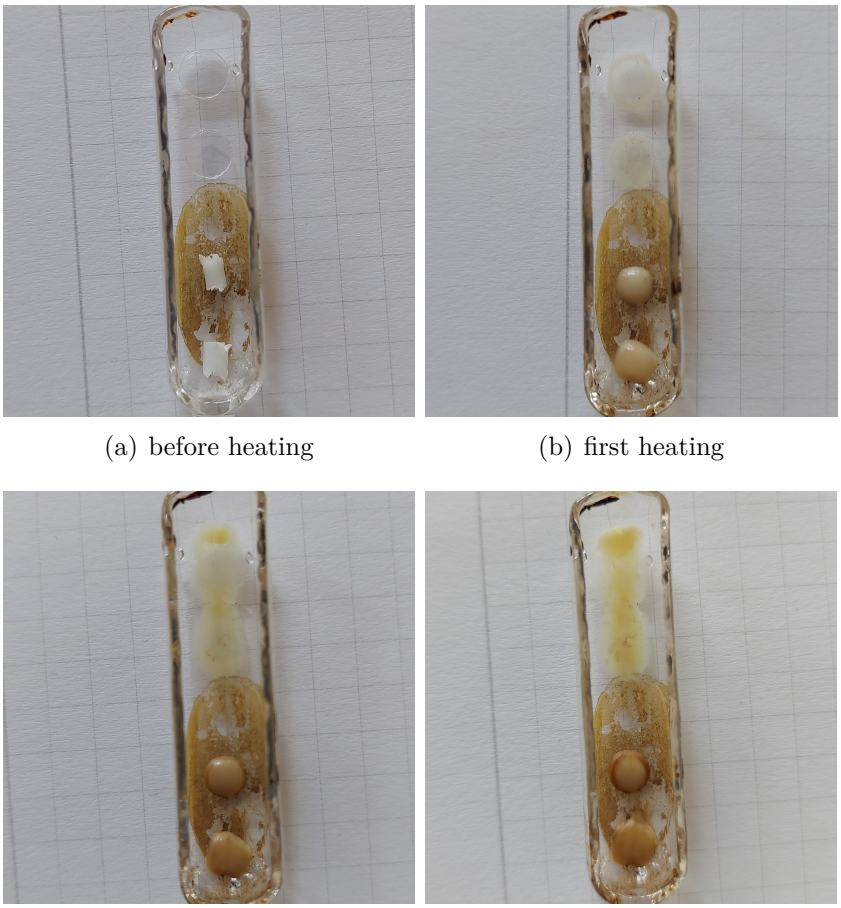

(a) before heating (b) first heating

(c) second heating (d) third heating

Figure 31: Multiple reheatings for both PET (bottom two samples) and cPET (top two samples) under air as carrier gas (40, 100 and 100 min). For reference, the background grid is 5 mm in width. (a) Starting condition before the heating. The brown spot on the glass crucible is a discoloration from a previous measurement, that is assumed to have no influence on the process. (b) Melted samples after the first heating. A slight color change is visible. (c) Samples after the second heating. The color change becomes stronger. (d) Samples after the final third heating. The PET pellets turn to a dark brown tone and the cPET pieces turn to an opaque yellow/brown tint.

are conducted similarly to the previous ones. For both samples, three consecutive heating and cooling cycles are executed. After each step, a picture is taken to monitor the process of discoloration. As both plastic samples do not exhibit any discoloration from the first to the third heating cycle, only the final results are shown in figure 32.

The high purity PET pellets again melt into large drops, but this time they keep their initial pure white color (fig. 32(a)). This melting happens right away at the very first heating, for all consecutive reheatings, no further change is observed. When comparing them to the

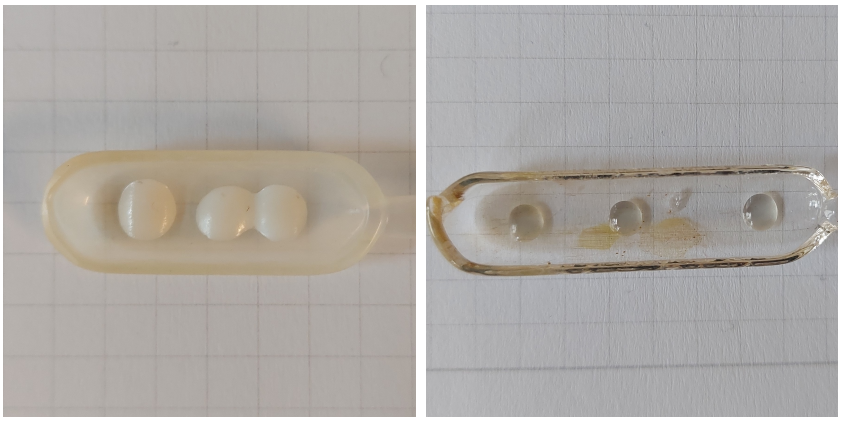

(a) PET pellets (b) cPET pieces

Figure 32: Final result of multiple reheatings (40, 100 and 100 min) for both PET and cPET under nitrogen gas. As no change during the reheatings is visible for the samples, only the final pictures are shown. For reference, the background grid is 5 mm in width. (a) PET sample after the final third heating. The pellets melt into large drops that keep their clean white color. (b) cPET sample after the final third heating. The pieces melt into tiny drops and keep their transparency.

melted pellets from the previous experiment under air, they look very much alike, besides the difference in color.

The cPET pieces also melt into droplets, but with a smaller diameter than in their initial form, as seen in figure 32(b). This also happens in the very first heating cycle. In this form, the sample is still transparent, but melted onto the glass crucible. This form stays constant for any further reheating procedure. Apart from the non-existing color change under nitrogen, the change of the melted plastic into the form of droplets is a new behavior that does not happen under air. As already mentioned when discussing the results of figure 30(d), the cPET pieces seem to keep their initial color/transparency when using nitrogen as carrier gas.

To gain a better overview of the changes involved when comparing air and nitrogen for both plastic samples, figure 33 shows a picture of all three glass crucibles used during multiple reheatings. The leftmost is the commodity cPET sample when using nitrogen, the middle one displays the commodity (top) and high purity samples (bottom) under air and the rightmost shows how the high purity PET pellets behave under nitrogen. This picture clearly illustrates the fact that PET/cPET samples do not undergo a color change when using non-oxidative nitrogen gas.

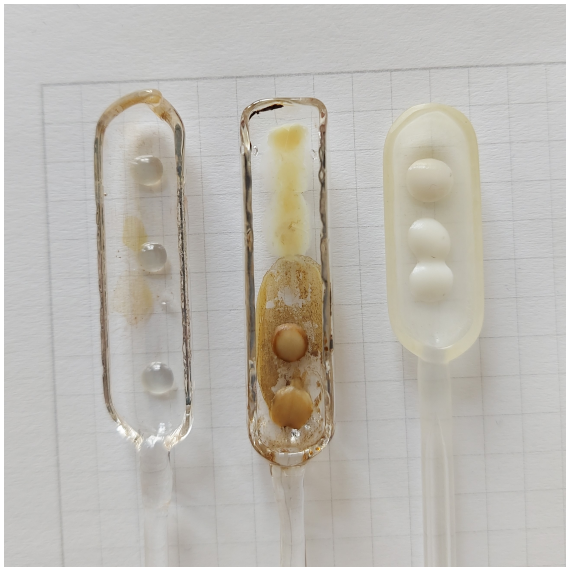

Figure 33: Glass crucibles showing the final results after three consecutive reheatings: the leftmost shows the commodity cPET sample when using nitrogen, the middle one the commodity (top) and high purity samples (bottom) under air and the rightmost the high purity PET pellets under nitrogen gas. For reference, the background grid is 5 mm in width.

Chapter 7

Conclusion

As shown in this thesis, polyethylene terephthalate plastic can create wide particle number size distributions in the range between 0 - 40 nm with high concentrations, up to a few 10^8 cm^{-3}. The experiments were based on the measurements by [1], verifying that PET and cPET plastics can actually create stable PNSDs at comparatively low temperatures. By changing different parameters in the measurement procedure, dependencies of the temperature, the flow and the sample amount could be found.

By changing the setpoint temperature of the tube furnace, the overall height of the PNSDs can be controlled, as a higher temperature positively correlates with higher peak concentrations. On the larger particle side, an increase of temperature also yields a wider distribution. This trend occurs for both kinds of plastic under both carrier gases. However, in the case of air, the temperature dependency is stronger pronounced for cPET plastic, and it develops a shoulder in the distribution. Under nitrogen gas, both plastics develop the same phenomenon, suggesting that some coagulation might take place. After all, the high concentrations in the range of 10^7 - 10^8 cm^{-3} could definitely lead to coagulation and therefore to the formation of a shoulder in the PNSDs.

The flow dependency has a far more complex behavior and establishes no clear trend throughout the measurements. In the case of cPET under air, the data implies an inverse flow dependency, meaning that a higher flow rate yields overall lower concentrations. This phenomenon could be explained by the fact that a higher flow rate corresponds to a higher cooling efficiency of the sample, thus lowering its temperature significantly. This could lead to lower particle concentrations in the aerosol. In all other cases, the temperatures to stabilize the PNSDs are spread so far apart that they already comprehend a temperature dependency that is probably the determining factor. Another interesting point is the behavior of the shoulder that forms during all flow measurements under nitrogen gas (PET and cPET) and the cPET measurement under air. In all of those three cases, it is observable that the

shoulder smears out and vanishes when the flow is reduced towards a value of 0.8 lpm. As mentioned before, a similar effect can be observed for the temperature measurements. The difference is, however, that the shoulder gets less pronounced, the more the temperature is increased. This supports the assumption that a lower flow rate through the tube furnace yields a stronger heated sample, thus increasing the sample temperature to a point where the shoulder smears out.

The dependency of the PNSDs when changing the initial sample amount takes again a similar trend as the temperature dependency, but far less pronounced: more sample material gives higher concentrations and wider distributions. However, a special case presents itself when taking measurements with high purity PET plastic. Under both carrier gases, the change from one single to multiple pellets yields a significant increase in the width of the distribution. For the commodity version, this is not observed. One possible explanation for this phenomenon could be a change in the position of the sample material on the glass crucible. Due to possible irregularities in the heating tube of the tube furnace, it could happen that one single sample pellet lies at a spot where the temperature is slightly lower than in the other places. For more material, as in the case of the cPET snippets, the sample is spread out evenly over the glass crucible. This could lead to a higher chance that at least one sample piece would lie at the maximum heating position, with the others distributed around it.

When comparing the obtained information with [1], one finds that the temperature dependency, as well as the sample amount dependency of the PNSDs, for the high purity PET sample under air as carrier gas are reproducible. The peak concentrations, as shown in [1], also fall into a similar range of 10^7 - $10^8\,\mathrm{cm}^{-3}$. However, a difference is found when comparing the actual values of the temperature range that generates a stable PNSD. As stated in [1], a sufficient temperature to create a stable distribution for PET (under air) is 220 °C, which is at least 10 - 20 °C colder than the lowest temperature of the first stable distribution of PET in this thesis. This is probably influenced by differences in the used tube furnaces.

By a direct comparison of the PNSD shapes, it was found that when using nitrogen as a carrier gas, a significant shift of the maximum peak towards lower particle diameters occurs. While the mode diameters under air are $d_m(\mathrm{PET}) = 12.4\,\mathrm{nm}$ and $d_m(\mathrm{cPET}) = 11.4\,\mathrm{nm}$, both with a geometric standard deviation of approximately 1.4 and a FWHM spread of 11.4 nm (PET) and 11.7 nm (cPET), they decrease to $d_m(\mathrm{PET}) = 6.9\,\mathrm{nm}$ and $d_m(\mathrm{cPET}) = 9.0\,\mathrm{nm}$ for nitrogen as carrier gas. In these cases, σ_g equals approximately 1.3 for both distributions with decreased FWHM values of 5.0 nm (PET) and 6.4 nm (cPET). This shows that the two different plastic samples develop different PNSDs under a non-oxidative carrier gas, when compared to air. This strengthens the assumption that the created aerosol particles could be of different chemical composition when comparing the two carrier gases.

At diameters of 4 - 10 nm, the concentration is enhanced up to a factor of ten. A nitrogen atmosphere therefore creates a smaller number of big particles, but a higher amount of smaller particles with an enhanced concentration. This effect is remarkably more prominent in the high purity PET version.

In addition to the PNSDs measurements, it was further shown that the cutoff diameter $d_{p,50}$ of the CPC is the main reason for the steep decline of all PNSDs on the lower end. One result of this thesis is that $d_{p,50}$ cannot be distinguished when measuring it for the two samples PET / cPET for one kind of carrier gas. By successfully measuring its value for both carrier gases, however, it was found that for nitrogen gas its value changes from around 3.8 nm (air) towards slightly larger diameters of approximately 4.5 nm (N_2).

This change barely yields a significant difference in the uncertainties, however, it might be linked to some sort of oxidation event that is happening under air, giving the (possibly) oxidized aerosol particles an enhanced activation efficiency over the not oxidized ones under nitrogen gas in a water-based CPC. It would be interesting to repeat the same measurements again, but this time with a butanol-based CPC, as the water-based model in this thesis was simply selected, because it was the only instrument available at that time. Under butanol, an oxidation process might be easier visible, as a change in the polarity could lead to stronger differences in the activation efficiency.

An interesting detail in the shape of the cutoff curves is the position of the plateau. Independent of the carrier gas in use or the respective plastic sample, the ratio always converges towards a value of approximately 80 %. The missing amount to the ideal value of 100 % could be explained by the differences in the structure of the measuring devices. As the CPC has many tubings that promote diffusion losses, a deviation from the expected perfect value will always be inherited by the measurements. However, if it was only lead by diffusion, the position of the plateau would be expected to rise on the larger particle diameter end. As this is not observed, there might still be some unknown source underlying this phenomenon.

Finally, it was shown that a significant discoloration process occurs for both plastics in air. This process is actually governed by the number of reheatings, while the heating duration plays a negligible role. As this discoloration process is never observed for any measurement under nitrogen gas, it further confirms the assumption that some oxidation process is involved when heating PET and cPET plastic.

To conclude, this thesis found a set of parameters that allows to control the overall shape of the PNSDs for a high purity and a commodity version, as well as strong indicators for an oxidation process under air. This provides valuable insights for possible further research.

Chapter 8

Future Research

The findings of this thesis yield new insights into the topic of PET microplastic. Further research, conducted based on this thesis, could follow a few different questions. One interesting point would be the use of a commodity plastic version of known composition. This knowledge could help with the interpretation of the results, as some differences in the behavior of the high purity version and the commodity version could possibly be explained.

The biggest question that arises from the results is if the aerosol particles are actually of the same or different chemical composition when switching the carrier gas air to a non-oxidative one, like nitrogen. This could potentially be investigated with mass spectrometry. New insights into this topic could lead to a better understanding of the general process of micro- and nanoplastic creation, yielding valuable information on how to possibly minimize the amount of its presence in the atmosphere.

Another interesting point could be to investigate the exact shape of the PNSDs on the lower end. This could be tried with a butanol-based CPC, or, as the cutoff diameter of the CPC is always the limiting factor, a nano-enhancer could theoretically be used to shift the diameters of the small particles towards sizes that can be detected by a standard CPC. This would yield additional insights into the lower end of the PNSDs. These insights could be crucial for further research regarding measuring devices for the detection of micro- and nanoplastics in the atmosphere. After all, we still do not know the lower size limit of the particle generation.

Finally, the same measurements could also be repeated, but for different kinds of plastic, such as polyethene, polypropene or polyvinyl chloride. A broad overview of the respective PNSDs and the differences, when reacting to a non-oxidative carrier gas, as well as the lower size limit of the particle generation would be crucial for further insights in this field of physics.

List of Tables

List of Figures

Bibliography

[1] P. J. Wlasits, A. Stoellner, G. Lattner, K. Maggauer, and P. M. Winkler, "Size characterization and detection of aerosolized nanoplastics originating from evaporated thermoplastics," *Aerosol Science and Technology*, vol. 56, no. 2, pp. 176–185, 2022.

[2] M. Aeschlimann, G. Li, Z. A. Kanji, and D. M. Mitrano, "Potential impacts of atmospheric microplastics and nanoplastics on cloud formation processes," *Nature geoscience*, vol. 15, pp. 967–975, 2022.

[3] P. J. Wlasits, R. Konrat, and P. M. Winkler, "Heterogeneous nucleation of supersaturated water vapor onto sub-10 nm nanoplastic particles," *Environmental Science & Technology*, vol. 57, no. 4, pp. 1584–1591, 2023.

[4] X. Chang, Y. Xue, J. Li, L. Zou, and M. Tang, "Potential health impact of environmental micro- and nanoplastics pollution," *Journal of applied toxicology*, vol. 40, no. 1, pp. 4–15, 2020.

[5] M. Teles, J. C. Balasch, M. Oliveira, J. Sardans, and J. Peñuelas, "Insights into nanoplastics effects on human health," *Science bulletin (Beijing)*, vol. 65, no. 23, pp. 1966–1969, 2020.

[6] M. S.-L. Yee, L.-W. Hii, C. K. Looi, W.-M. Lim, S.-F. Wong, Y.-Y. Kok, B.-K. Tan, C.-Y. Wong, and C.-O. Leong, "Impact of microplastics and nanoplastics on human health," *Nanomaterials (Basel, Switzerland)*, vol. 11, no. 2, 2021. [Online]. Available: https://doi.org/10.3390/nano11020496

[7] G. M. Zarus, C. Muianga, C. M. Hunter, and R. S. Pappas, "A review of data for quantifying human exposures to micro and nanoplastics and potential health risks," *Science of the total environment*, vol. 756, 2021. [Online]. Available: https://doi.org/10.1016/j.scitotenv.2020.144010

[8] P. J. Wlasits, D. Stolzenburg, C. Tauber, S. Brilke, S. H. Schmitt, P. M. Winkler, and D. Wimmer, "Counting on chemistry: laboratory evaluation of seed-material-dependent detection efficiencies of ultrafine condensation particle counters," *Atmospheric Measurement Techniques*, vol. 13, no. 7, pp. 3787–3798, 2020.

[9] C. B. Crawford, *Microplastic pollutants.* Amsterdam, Netherlands: Elsevier, 2017.

[10] V. K. Stokes, *Introduction to Plastics Engineering.* Glasgow, UK: John Wiley & Sons Ltd, 2020.

[11] S. Pickering, "Recycling technologies for thermoset composite materials—current status," *Composites. Part A: applied science and manufacturing*, vol. 37, no. 8, pp. 1206–1215, 2006.

[12] "Safety data sheet," Sigma-Aldrich, April 2022, Accessed: Dez. 15, 2023. [Online]. Available: https://www.sigmaaldrich.com/AT/de/product/aldrich/429252#product-documentation

[13] H. Masai, T. Nishibe, S. Yamamoto, T. Niizuma, N. Kitamura, T. Akai, T. Ohkubo, and M. Yoshida, "Low melting oxide glasses prepared at a melt temperature of 500 °C," *Scientific reports*, vol. 11, no. 1, 2021. [Online]. Available: https://doi.org/10.1038/s41598-020-80424-9

[14] I. Ali, X. Tan, J. Li, C. Peng, P. Wan, I. Naz, Z. Duan, and Y. Ruan, "Innovations in the development of promising adsorbents for the remediation of microplastics and nanoplastics – a critical review," *Water research (Oxford)*, vol. 230, 2023. [Online]. Available: https://doi.org/10.1016/j.watres.2022.119526

[15] A. E. Alprol, M. S. Gaballah, and M. A. Hassaan, "Micro and nanoplastics analysis: Focus on their classification, sources, and impacts in marine environment," *Regional studies in marine science*, vol. 42, 2021. [Online]. Available: https://doi.org/10.1016/j.rsma.2021.101625

[16] C. Guerranti, T. Martellini, G. Perra, C. Scopetani, and A. Cincinelli, "Microplastics in cosmetics: Environmental issues and needs for global bans," *Environmental toxicology and pharmacology*, vol. 68, pp. 75–79, 2019.

[17] B. Singh and N. Sharma, "Mechanistic implications of plastic degradation," *Polymer degradation and stability*, vol. 93, no. 3, pp. 561–584, 2008.

[18] H. K. Webb, J. Arnott, R. J. Crawford, and E. P. Ivanova, "Plastic degradation and its environmental implications with special reference to poly(ethylene terephthalate)," *Polymers*, vol. 5, no. 1, pp. 1–18, 2013.

[19] I. Vollmer, H. Sardon, G. W. Huber, and Z. Li, "Introduction to plastic conversion," *Polymer chemistry*, vol. 14, no. 26, pp. 3054–3056, 2023.

[20] "Plastics - the fast facts 2023," Plastics Europe AISBL, 2023, Accessed: Feb. 24, 2024. [Online]. Available: https://plasticseurope.org/knowledge-hub/plastics-the-fast-facts-2023/

[21] I. A. Kane and M. A. Clare, "Dispersion, accumulation, and the ultimate fate of microplastics in deep-marine environments: A review and future directions," *Frontiers in earth science (Lausanne)*, vol. 7, 2019. [Online]. Available: https://doi.org/10.3389/feart.2019.00080

[22] J. P. Barreiros and J. Barcelos, "Plastic ingestion by a leatherback turtle dermochelys coriacea from the azores (NE Atlantic)," *Marine pollution bulletin*, vol. 42, no. 11, pp. 1196–1197, 2001.

[23] I. Sazima, O. B. F. Gadig, R. C. Namora, and F. S. Motta, "Plastic debris collars on juvenile carcharhinid sharks (rhizoprionodon lalandii) in southwest Atlantic," *Marine pollution bulletin*, vol. 44, no. 10, pp. 1147–1149, 2002.

[24] L. K. Blight and A. E. Burger, "Occurrence of plastic particles in seabirds from the eastern north Pacific," *Marine pollution bulletin*, vol. 34, no. 5, pp. 323–325, 1997.

[25] D. Klingelhöfer, M. Braun, D. Quarcoo, D. Brüggmann, and D. A. Groneberg, "Research landscape of a global environmental challenge: Microplastics," *Water research (Oxford)*, vol. 170, 2020. [Online]. Available: https://doi.org/10.1016/j.watres.2019.115358

[26] M. Bergmann, S. Mützel, S. Primpke, M. B. Tekman, J. Trachsel, and G. Gerdts, "White and wonderful? Microplastics prevail in snow from the Alps to the Arctic," *Science advances*, vol. 5, no. 8, 2019. [Online]. Available: https://www.science.org/doi/10.1126/sciadv.aax1157

[27] K. Zhang, J. Su, X. Xiong, X. Wu, C. Wu, and J. Liu, "Microplastic pollution of lakeshore sediments from remote lakes in Tibet plateau, China," *Environmental pollution*, vol. 219, pp. 450–455, 2016.

[28] S. Allen, D. Allen, V. R. Phoenix, G. Le Roux, P. D. Jiménez, A. Simonneau, S. Binet, and D. Galop, "Atmospheric transport and deposition of microplastics in a remote mountain catchment," *Nature geoscience*, vol. 12, no. 5, pp. 339–344, 2019.

[29] R. Sharma and H. Kaushik, "Micro-plastics: An invisible danger to human health," *CGC International Journal of Contemporary Technology and Research*, vol. 3, no. 2, pp. 182–186, 2021, Accessed: Jan. 02, 2024. [Online]. Available: http://cgcijctr.com/download.php?file=CGCIJCTR_C0302107.pdf

[30] Y. Lee, J. Cho, J. Sohn, and C. Kim, "Health effects of microplastic exposures: Current issues and perspectives in South Korea," *Yonsei medical journal*, vol. 64, no. 5, pp. 301–308, 2023.

[31] J. Windheim, L. Colombo, N. C. Battajni, L. Russo, A. Cagnotto, L. Diomede, P. Bigini, E. Vismara, F. Fiumara, S. Gabbrielli, A. Gautieri, G. Mazzuoli-Weber, M. Salmona, and L. Colnaghi, "Micro- and nanoplastics' effects on protein folding and amyloidosis," *International Journal of Molecular Sciences*, vol. 23, no. 18, 2022. [Online]. Available: https://doi.org/10.3390/ijms231810329

[32] J. H. Seinfeld and S. N. Pandis, *Atmospheric chemistry and physics: from air pollution to climate change*, 3rd ed. Hoboken, New Jersey: Wiley, 2016.

[33] W. C. Hinds and Y. Zhu, *Aerosol technology: properties, behavior, and measurement of airborne particles*, 3rd ed. New York: John Wiley & Sons, Ins., 2022.

[34] G. Steiner, "High resolution mobility spectrometry of molecular ions and their effect on the charging probabilities of airborne particles under bipolar diffusion charging conditions," Dr. rer. nat. dissertation, Universität Wien, Vienna, Austria, 2011, Accessed: Mar. 03, 2023. [Online]. Available: https://utheses.univie.ac.at/detail/13233

[35] P. Kulkarni, P. A. Baron, and K. Willeke, *Aerosol measurement: principles, techniques, and applications*, 3rd ed. Hoboken, New Jersey: Wiley, 2011.

[36] G. Voss, "Teil 9: Die mittlere freie Weglänge von Gasteilchen und die Viskosität von Gasen," *Vakuum in Forschung und Praxis. Spezailthema: Vakuummesstechnik*, vol. 31, no. 4, pp. 40–42, 2019. [Online]. Available: https://doi.org/10.1002/vipr.201970405

[37] P. Gonugunta, "Synthesis and characterization of biobased carbon nanoparticles from lignin," A thesis presented to the university of Guelph, Ontario, Canada, 2012, Accessed: Feb. 24, 2024. [Online]. Available: http://hdl.handle.net/10214/3608

[38] P. Kallinger and W. W. Szymanski, "Experimental determination of the steady-state charging probabilities and particle size conservation in non-radioactive and radioactive bipolar aerosol chargers in the size range of 5–40 nm," *Journal of nanoparticle research: an interdisciplinary forum for nanoscale science and technology*, vol. 17, no. 4, 2015, Accessed: Jan. 02, 2024. [Online]. Available: https://pubmed.ncbi.nlm.nih.gov/25866470/

[39] N. A. Fuchs, "On the stationary charge distribution on aerosol particles in a bipolar ionic atmosphere," *Pure and applied geophysics*, vol. 56, no. 1, pp. 185–193, 1963. [Online]. Available: https://doi.org/10.1007/BF01993343

[40] G. Steiner and G. P. Reischl, "The effect of carrier gas contaminants on the charging probability of aerosols under bipolar charging conditions," *Journal of aerosol science*, vol. 54, no. 7, pp. 21–31, 2012.

[41] A. Wiedensohler, "An approximation of the bipolar charge distribution for particles in the submicron size range," *Journal of Aerosol Science*, vol. 19, no. 3, pp. 387–389, 1988, Accessed: Feb. 03, 2024. [Online]. Available: https://www.sciencedirect.com/science/article/pii/0021850288902789

[42] R. C. Flagan, "On differential mobility analyzer resolution," *Aerosol Science and Technology*, vol. 30, no. 6, pp. 556–570, 1999.

[43] "Nano water-based condensation particle counter (N-WCPC) model 3788 - specification sheet," TSI Incorporated, 2012, Accessed: Dez. 15, 2023. [Online]. Available: https://tsi.com/getmedia/b3aa9539-222f-4799-a342-ba9ff4510a3b/3788_5001340_Web?ext=.pdf

[44] "Nano water-based condensation particle counter model 3788 - operation and service manual," TSI Incorporated, 2012, Accessed: Dez. 15, 2023. [Online]. Available: https://www.kenelec.com.au/wp-content/uploads/2016/06/TSI_3788_Condensation_Particle_Counter_Manual.pdf

[45] S. Tran, K. Iida, K. Yashiro, Y. Murashima, H. Sakurai, and J. S. Olfert, "Determining the cutoff diameter and counting efficiency of optical particle counters with an aerodynamic aerosol classifier and an inkjet aerosol generator," *Aerosol science and technology*, vol. 54, no. 11, pp. 1335–1344, 2020.

[46] M. R. Stolzenburg and P. H. McMurry, "An ultrafine aerosol condensation nucleus counter," *Aerosol science and technology*, vol. 14, no. 1, pp. 48–65, 1991.

[47] "Aerosol electrometer model 3068B," TSI Incorporated, 2022, Accessed: Dez. 17, 2023. [Online]. Available: https://tsi.com/getmedia/a879704c-938f-4564-b13f-f19ad77667f0/3068B-Spec-Sheet?ext=.pdf

[48] K. Pihlava, J. Keskinen, and J. Yli-Ojanperä, "Improving the signal-to-noise ratio of faraday cup aerosol electrometer based aerosol instrument calibrations," *Aerosol science and technology*, vol. 50, no. 4, pp. 373–379, 2016.

[49] A. Järvinen, J. Keskinen, and J. Yli-Ojanperä, "Extending the faraday cup aerosol electrometer based calibration method up to 5 µm," *Aerosol science and technology*, vol. 52, no. 8, pp. 828–840, 2018.

[50] P. M. Winkler, G. Steiner, A. Vrtala, H. Vehkamäki, M. Noppel, K. E. J. Lehtinen, G. P. Reischl, P. E. Wagner, and M. Kulmala, "Heterogeneous nucleation experiments bridging the scale from molecular ion clusters to nanoparticles," *Science*, vol. 319, no. 5868, pp. 1374–1377, 2008. [Online]. Available: https://www.science.org/doi/abs/10.1126/science.1149034

[51] A. Kupc, O. Bischof, T. Tritscher, M. Beeston, T. Krinke, and P. E. Wagner, "Laboratory characterization of a new nano-water-based CPC 3788 and performance comparison to an ultrafine butanol-based CPC 3776," *Aerosol science and technology*, vol. 47, no. 2, pp. 183–191, 2013.

[52] D. Stolzenburg, G. Steiner, and P. M. Winkler, "A dma-train for precision measurement of sub-10 nm aerosol dynamics," *Atmospheric measurement techniques*, vol. 10, no. 4, pp. 1639–1651, 2017.

Appendix A

Python Code

```
import matplotlib.pyplot as plt
import numpy as np
import pandas as pd
import math
import csv
from datetime import datetime, timedelta
import os

#calculate Cunningham slip correction factor
def C_s(mfp0, d):
    a1 = 2.492
    a2 = 0.84
    a3 = 0.43
    C = 1 + a1 * (mfp0 / d) + a2 * (mfp0 / d) * math.exp(-a3 * (d / mfp0))
    return C

#calculate DMA inversion
def DMA_inversion(V, start, acc, mfp0, Q_DMA_0, eta):
    R_i = 17.5 #inner radius of DMA in mm
    R_o = 24.1 #outer radius of DMA in mm
    L = 0.015  #length of the DMA in m
    Q = Q_DMA_0 / 60. / 1000. #DMA sheath flow conversion of lpm to m3/s
    e = 1.602176634e-19       #elementary charge in C

    const = (2. / 3.) * (e * L) / (Q * eta * math.log(R_o / R_i))
    iterator = const * C_s(mfp0, start) * V
    dummy = 0.



```

```
    while True:
        if abs(iterator - dummy) < acc:
            break
        else:
            dummy = iterator
            iterator = const * C_s(mfp0, iterator) * V

    return iterator
```

Code Listing A.1: Part of the Python code that computes the DMA inversion. The dimensions of the DMA are hardcoded together with the inversion in the function *DMA_inversion*, while the Cunningham slip correction factor C_s is defined in an additional function called *C_s*.

Appendix B

Cutoff Data for the CPC in Air

Table B.1: Summarized cutoff values with their belonging errors for measurements under air, as seen in figure 27.

PET			cPET		
d_p (nm)	η ( )	$\eta_{err.}$ ( )	d_p (nm)	η ( )	$\eta_{err.}$ ( )
3.41	0.149	0.011	2.58	4.5E-04	2.7E-04
3.65	0.359	0.025	2.77	0.0122	0.0022
3.92	0.605	0.049	2.97	0.092	0.013
4.21	0.677	0.027	3.18	0.276	0.047
4.51	0.699	0.038	3.41	0.427	0.055
4.84	0.712	0.062	3.65	0.460	0.028
5.19	0.724	0.030	3.92	0.550	0.041
5.56	0.738	0.043	4.21	0.651	0.046
6.06	0.745	0.078	4.51	0.716	0.039
8.08	0.790	0.084	4.84	0.752	0.037
10.06	0.785	0.082	5.19	0.767	0.028
12.06	0.807	0.096	5.56	0.771	0.035
-	-	-	6.06	0.777	0.053
-	-	-	8.08	0.792	0.029
-	-	-	10.06	0.802	0.073
-	-	-	12.06	0.809	0.085
-	-	-	15.14	0.812	0.071

Appendix C

Cutoff Data for the CPC in Nitrogen Gas

Table C.1: Summarized cutoff values with their belonging errors for measurements under nitrogen gas, as seen in figure 28.

PET			cPET		
d_p (nm)	η ( )	$\eta_{err.}$ ( )	d_p (nm)	η ( )	$\eta_{err.}$ ( )
2.60	4.3E-06	8.9E-06	2.59	3.4E-04	3.9E-04
3.00	2.9E-06	4.9E-06	2.99	7.0E-05	7.1E-05
3.21	1.03E-04	3.4E-05	3.20	5.1E-05	4.6E-05
3.45	1.58E-03	2.1E-04	3.43	5.7E-04	1.4E-04
3.69	0.0259	0.0029	3.67	0.01046	9.7E-04
3.96	0.1682	0.0073	3.94	0.0897	0.0078
4.25	0.407	0.029	4.23	0.302	0.012
4.55	0.589	0.049	4.54	0.518	0.037
4.89	0.697	0.093	4.87	0.652	0.030
5.24	0.77	0.21	5.22	0.715	0.027
5.61	0.76	0.10	5.59	0.749	0.067
6.13	0.88	0.30	6.10	0.785	0.094
8.16	0.84	0.16	8.13	0.81	0.17
10.16	0.82	0.16	10.12	0.810	0.067
12.19	0.83	0.12	12.14	0.85	0.20
15.30	0.84	0.11	-	-	-